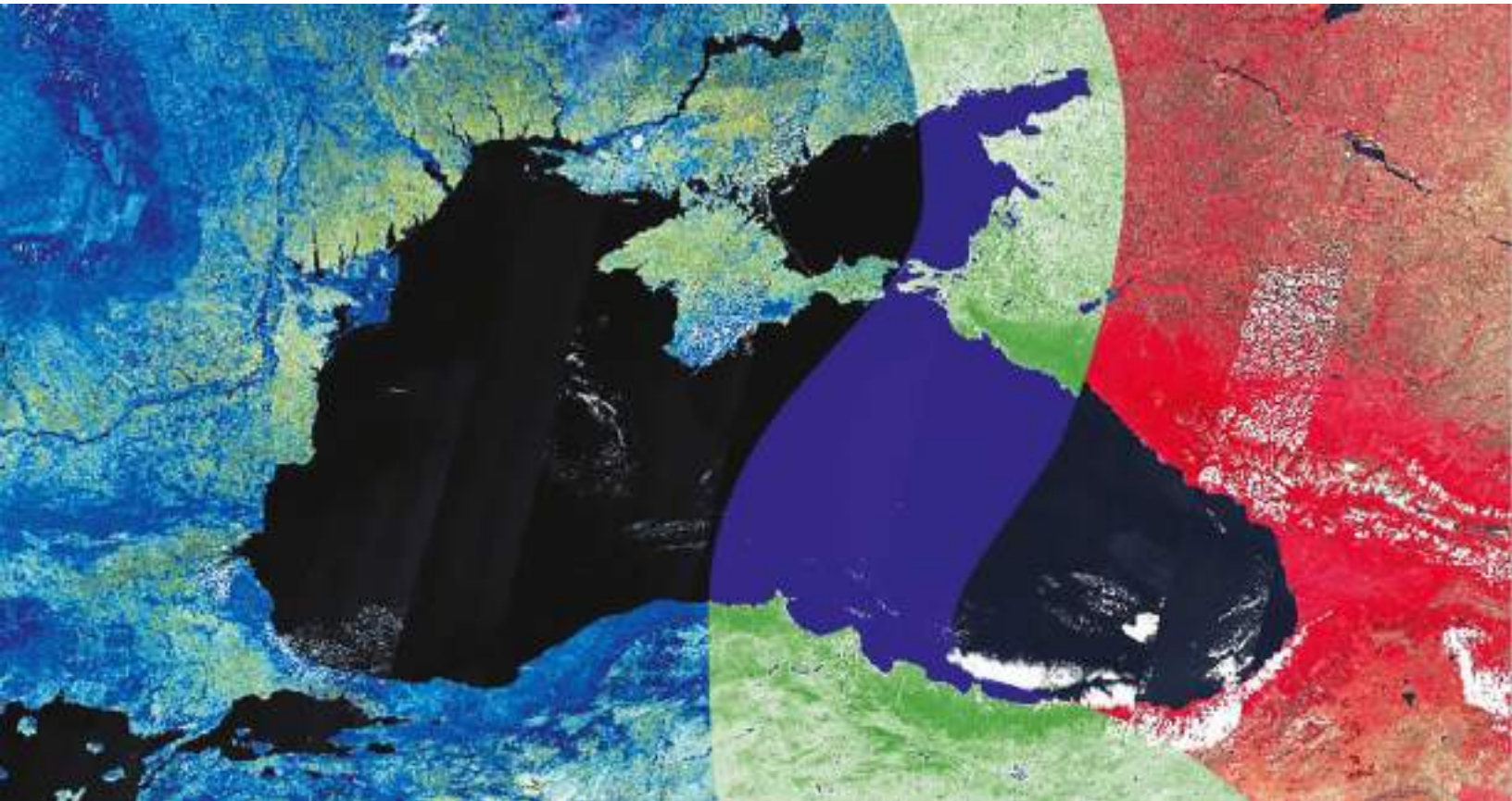


Copernicus assisted environmental monitoring across the Black Sea Basin - PONTOS



Report on Dynamics of Coastal Line Changes

Deliverable D.T1.2.1

PONTOS-GR (Greece)

Coastal Erosion assessment along the Nestos River Delta



Table of Contents

Introduction	4
Methodological Concept Description	7
Data collection	9
Topographic data	9
Land cover data	10
Hydrological data	10
Oceanographic Data	11
Data collection lists	12
Satellite images	13
Earth Explorer (Landsat 4-5 TM and Landsat 8 OLI)	13
Sentinel 2 Mission	14
Coastal erosion analysis methodology by processing historical satellite images	16
Satellite image selection	16
Coastline extraction from satellite images	17
Evaluation of the shoreline evolution	18
Validation of the satellite image classification method	19
Wave data	22
Peaks Over Threshold analysis	23
Expected exceedance	23
Poisson + GPD = GEV	24
Declustering	25
Wave Characteristics at the Nearshore and Breaker Zone and Incident Wave Energy Calculation	26
Study Site Description	28
Geomorphology and Bathymetry	29
Land Cover Data	33
River Discharge Data	34
Wave analysis	35



Wave time series analysis	35
Results of CMEMS extreme Wave data analysis	39
The Ray-Wave Model	41
Coastal Erosion Analysis Results.....	42
West Study site (Vasova lagoon - Agiasma Beach)	45
Gulf of Keramoti	52
West Nestos Estuaries.....	59
East Nestos.....	66
References	76

Introduction

The coastal zone is a dynamic geomorphologic system in which multiple changes occur at diverse temporal and spatial scales (Mills et al., 2005), mostly affecting the shoreline position response through erosion/deposition actions, resulting from natural and anthropogenic activities (Van Rijn, 1993). Natural effects include shoreline interactions with incident waves, tides, storms, tectonic processes, and sediment loads reaching the coastal zone through the hydrologic network of the adjacent watershed (Dolan et al., 1981). Anthropogenic effects are mainly related to the impacts of human activities or interventions along the coastal zone, like the mismanagement of coastal structures, dredging activities, dam construction upstream a river, intense tourism activity, overpopulation, etc. (Williams et al., 2018). In parallel, climate change is expected to induce further pressure on coastlines due to Sea Level Rise (SLR) effect and the increase in storminess (Zhang et al., 2004). Coastal authorities are faced with the increasingly complex task of balancing development and managing coastal vulnerabilities and risks (Salman et al., 2004). In that sense, the Integrated Coastal Zone Management (ICZM) provides a framework to resolve conflicts, mitigate impacts of short-/long-term uses, and support strategies for sustainable coastal management (Anfuso et al., 2011).

Coastal zone monitoring is an essential task for national/regional development and environmental protection, in which the assessment of the state of historic shorelines is critical (Rasuly et al., 2010). Various data types have been considered for monitoring the shoreline change, either using direct (i.e., GPS, Topographic lasers) or indirect (i.e., aerial photography, airborne LiDAR, satellite images) techniques. Using in-situ observation techniques, such as the highly-accurate GPS surveys (Morton et al., 1993; Harley et al., 2010) or the very precise terrestrial laser scanners (Saye et al., 2005; Theuerkauf and Rodriguez, 2012; Lee et al., 2013), the scientist may accomplish highly-accurate assessments. However, such measurements are costly and time-consuming, especially to map broad areas, and do not provide orthophotos useful in detecting specific terrain elements. Moreover, these techniques are inherently limited in temporal coverage, typically being either too short to identify long-term trends or too widely spaced in time to distinguish the short-term seasonal changes (Natesan et al., 2013).

Other techniques employ remotely sensed data as aerial photographs and webcam images (Hapke and Richmond, 2000; Alexander and Holman, 2004; Kroon et al., 2007; Taborda and Silva, 2012; Turki et al., 2013), and airborne LiDAR mapping (Stockdon et al., 2002; Young and Ashford, 2006; Pye and Blott, 2016). Recently, new survey techniques based on remotely piloted aircraft systems (RPAS, also called unmanned aerial vehicles, UAVs, or drones) have begun to be employed in geomorphological and

ecological studies (Everaerts, 2008; Anderson and Gaston, 2013; Colomina and Molina, 2014; Floreano and Wood, 2015), and become common survey tools in geosciences. The techniques described above cover larger areas over shorter time intervals, but their main limitations are their relatively costly and the commonly insufficient availability of images spanning periods of interest.

On the other hand, satellite imagery can combine moderate spatial resolution with broad spatial coverage and short-time scale in repeated measurements. It also has the potential advantage of allowing exploration of shoreline change in remote places with limited coastal information. Satellite imagery has been developed rapidly over the past few decades in terms of spatial resolution, frequency of passage over the exact location, and overall availability. Historical satellite images cover over 30 years with high spatial resolution.

There are several open-source databases for retrieving satellite images, such as:

- **Earth Explorer** (<https://earthexplorer.usgs.gov/>)
- **Copernicus Open Access Hub** (<https://scihub.copernicus.eu/>), and
- **Planet Explorer** (<https://www.planet.com/explorer/>).

Furthermore, remote sensing information can be integrated with Geographical Information Systems (GIS), as a helpful tool for analyzing and extracting more reliable and consistent information by using satellite imagery as base data (Louati et al., 2015).

In recent years, remote sensing data from high-resolution satellite sensors (i.e., Landsat, Sentinel, IKONOS, RapidEye, PlanetScope, etc.) have been used in several studies for automatic or semi-automatic shoreline extraction and shoreline position mapping. Shoreline delineation techniques, such as threshold level slicing or multi-spectral image classification, applied using panchromatic images, a single band or multiple bands combined may be used for various indices estimation (e.g., NDWI, mNWDI, NDVI) (Frazier and Page, 2000; Braud and Feng, 1998; Kuleli, 2010; Kuleli et al., 2011; Bouchahma and Yan, 2012). The satellite image processing methods to extract the shoreline position are applied using Geographical Information System software (e.g., QGIS, ArcGIS). All techniques have advantages and disadvantages and produce errors and uncertainties; for this reason, the user should validate the applied technique's accuracy (Frazier and Page, 2000). Several methods have been documented to evaluate the shoreline movement, mainly with the use of GIS software. The most common are the transect-based and the point-based approaches. Both techniques are capable of calculating the short- and long-term shoreline changes. Extraction and application of the transect-based process became more easily applied with the Digital Shoreline Analysis



System (DSAS), created by the United States Geological Survey USGS (Thieler et al., 2009).

The present report presents the methodology and the results of the coastal erosion assessment applied in the study sites of the PONTOS project. The shoreline change analysis covers the period from 1985 to 2020. The standard methodology was applied into four steps:

- a) the creation of a data-list with all satellites and satellite images available referring to the coastal area of interest,
- b) the historical shoreline extraction from the relevant satellite images,
- c) the evaluation of the shoreline movement throughout the study period, and
- d) the offshore and nearshore wave analysis (extreme wave events, incident wave energy, longshore sediment transport, etc.)

Methodological Concept Description

The herein-defined methodology will be eventually applied to all PONTOS pilot areas (Armenian, Georgian, Greek, and Ukrainian). This methodology entails the procedure of shoreline delineation using a semi-automatic image classification technique. All historical shorelines at all PONTOS pilot areas will be extracted by processing satellite images from Landsat 4-5 TM, Landsat 8 OLI, and Sentinel 2 satellite sensors. The historical image selection will be based on the correct geo-reference and the image clarity from the cloud cover. Then, the historical satellite images will be classified to distinguish land and water, and the historic shorelines will be extracted. The evaluation of the shoreline evolution will be performed using the Digital Shoreline Analysis System (DSAS), provided by the United States Geological Survey (USGS), capable to produce auto-generated transects. The methodology was validated using a GeoEye-1 satellite imagery having very high spatial resolution (0.46 m in panchromatic).

In parallel, using a series of algorithms, data from existing oceanographic databases describing coastal currents and waves were retrieved from external platforms and systems (e.g., from CMEMS). These data were further analyzed:

- a) to assess extreme waves (e.g., POT, EVA),
- b) to perform circular wave statistics, and finally,
- c) to apply a Ray Wave Model from the open sea to the nearshore zone computing all wave characteristics at the wave breaker and estimating the wave-induced nearshore current and the theoretical wave-induced sediment transport.

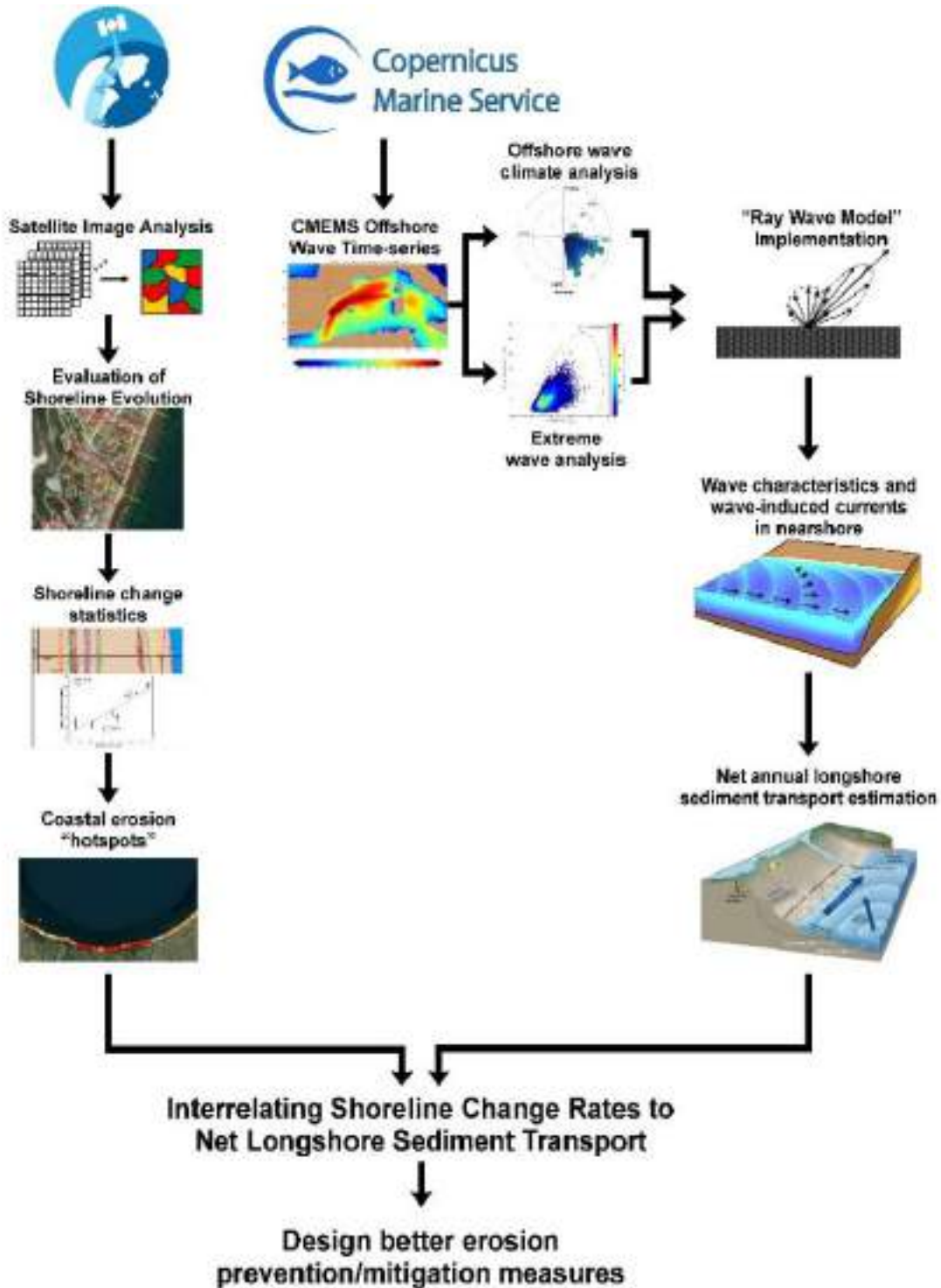


Figure 1. Conceptual framework to assess coastal erosion, identify the processes responsible for coastline changes, and design better prevention/mitigation measures.

Data collection

Topographic data

Topographic data adjacent to the examined shoreline catchment were retrieved from the Advanced Land Observation Satellite (ALOS) Global Digital Surface Model. This dataset is a global digital surface model (DSM) with horizontal resolution of approximately 30 m (basically ~1 arcsecond) produced by the Panchromatic Remote-sensing Instrument for Stereo Mapping (PRISM), which is an optical sensor on board the “ALOS” platform (Takaku et al. 2014).

Bathymetric data at the nearshore and the offshore of the study area were retrieved from two different databases. Initially, bathymetry data were retrieved from the Bathymetry portal of the European Marine Observation and Data Network (EMODnet) (<http://www.emodnet-bathymetry.eu>). Moreover, bathymetric survey data and aggregated bathymetry data sets were collated from public and research organizations for each maritime region. These data were further processed, quality controlled and used to produce the regional Digital Terrain Models (rDTMs). After that, these data could be integrated into the EMODnet DTM for the European seas.

The 2018 DTM version has a grid size of $1/16 \times 1/16$ arc minutes, where each grid cell has the following information:

- x, y coordinates,
- minimum water depth (m),
- average water depth (m),
- maximum water depth (m),
- the standard deviation of water depth (m),
- number of values used for interpolation over the grid cell,
- interpolation flag (identification of extrapolated cells),
- average water depth smoothed by means of a spline function (m),
- an indicator of the offsets between the average and smoothed water depth as the percentage of the water depth,
- reference to the prevailing source of data with metadata.

The DTM values have been determined from 4 possible sources of data:

1. **Bathymetric survey data:** high-resolution data sets from single and multibeam surveys that are referenced via the CDI Data Discovery and Access service,
2. **Digital Terrain Model data:** composite data sets produced and delivered by a number of external data providers, such as the Hydrographic Offices and their

internal bathymetric databases based upon previous surveys. The aggregated data sets were referenced via the Sextant Catalogue service,

3. **Satellite Derived Bathymetry data:** composite data sets produced from Landsat 8 images, in particular for the coastal stretches in Greece and Spain. The SDB data sets are referenced via the Sextant Catalogue service, and
4. **GEBCO 2014 30” gridded data**, used to complete area coverage in case there are no survey data or composite data sets available to the partners.

Land cover data

The CORINE Land Cover (CLC) is one of the most well-known and widely-used products retrieved from the Copernicus Land Monitoring Service. There are many editions previously produced (1990, 2000, 2006, and 2012), but the 2018 edition was used in the present study. It consists of an inventory of land cover in 44 classes. CLC uses a Minimum Mapping Unit (MMU) of 25 hectares (ha) for areal phenomena and a minimum width of 100 m for linear phenomena. The time series is complemented by change layers, highlighting changes in land cover with an MMU of 5 ha. Different MMUs mean that the change layer has a higher resolution than the status layer. Due to differences in MMUs, the difference between the two status layers will not be equal to the corresponding CLC-Changes layer. It is produced with assistance from the European Environment Agency’s Eionet network, which contributed their data, collected mainly by visual interpretation of high-resolution satellite imagery. In a few countries, semi-automatic solutions are applied, using national in-situ data, satellite image processing, GIS integration, and generalization. CLC has a wide variety of applications, underpinning various Community policies in the domains of environment, including agriculture, transport, spatial planning, etc.

Hydrological data

Historical hydrologic data were be retrieved from the Swedish Hydrometeorological Institute (SMHI), specifically from the database developed entitled Hydrological Predictions for the Environment (HYPE). HYPE model is a dynamic, semi-distributed, and process-based hydrological and nutrient transport model (Lindström et al., 2010) that can be used to assess water quantity and quality on a small and large scale. The HYPEweb, created by regulating HYPE model for pan-European basins, calculates water balance, hydrological processes (snow, glaciers, soil moisture, flow path, the contribution of groundwater and lakes), and sea discharges for the area from the British Isles to the Ural Mountains, Norway to the Mediterranean (9.6 million km²). The e-HYPE is an operational high-resolution model that generates data with a daily time step. The internal model components are checked and calibrated with observational data in different areas. The e-

HYPE system simulates the flow and provides topographical, precipitation, temperature, evapotranspiration, land cover, soil type, lake, river network-basins, and flow data used in modeling from global/continental databases and satellite products. The HYPEweb is an open-access web service, allowing any user to download daily flow rates (m^3/s) for any sub-basin across Europe. The model used to study the effects of climate and land-use change on water resources can also be considered in operational runoff forecasting studies for the early warning service and the hydropower sector. Using reliable quality input data, the model undergoes calibration and verification processes according to sound scientific principles (Arheimer et al., 2011).

Oceanographic Data

Physical and marine biogeochemical components are useful for coastal water quality monitoring and pollution control. Sea level rise is a key indicator of climate change affecting coastal erosion. Currents and waves play a crucial role in determining the impact of water circulation on coastal erosion. Global sea surface temperature is expected to rise by approximately $0.4 - 1.1^\circ C$ by 2025, with direct consequences on marine ecosystems and the appearance of tropical cyclones. Chlorophyll-a and Suspended Particulate Matter (SPM) are two of the most significant parameters for monitoring the impact of the rivers in the study area. Therefore, the retrieval of these datasets appears to be necessary to understand cost-effectively the underlying processes. The datasets retrieval was carried out through the Copernicus Marine Environment Monitoring Service (CMEMS), part of the Copernicus Program, which is an EU Program managed by the European Commission (EC) and implemented in partnership with the Member States, the European Space Agency (ESA), the European Organization for the Exploitation of Meteorological Satellites (EUMETSAT), the European Centre for medium-range Weather Forecasts (ECMWF), EU Agencies and Mercator Ocean. The program aimed at developing a set of European information services, based on satellite Earth Observation and in-situ (non-space) data.

The Copernicus Marine Environment Monitoring Service provides regular and systematic information about the physical state and dynamics of the ocean and marine ecosystems for the global ocean and the European regional seas. This data covers the analysis of the current condition, short-term forecasts of the conditions a few days in advance, and the provision of retrospective data records (re-analysis datasets). Many of the data delivered by the service (e.g., water temperature, salinity, sea level, currents, wind, and sea ice) also play a crucial role in the domain of weather, climate, and seasonal forecasting.

Data collection lists

A list of the data products, characteristics, and sources used for the present coastal erosion assessment in the Greek PONTOS pilot site is given in Table 1.

Table 1. List of the data products used for the coastal erosion assessment of the Greek PONTOS site and their attributes.

No	Data Products	Description	Number of items	Resolution	Period cover	Type of file / Format	Source	Link
1	Landsat 4-5 TM	Historical Satellite images	5	30 m	1985 to 2015	Raster (geotiff)	Earth Explorer	https://earthexplorer.usgs.gov/
2	Landsat 8 OLI	Historical Satellite image	1	30 m	2015	Raster (geotiff)	Earth Explorer	https://earthexplorer.usgs.gov/
3	Sentinel 2	Historical Satellite images	6	10 m	2015 to 2020	Raster (geotiff)	Copernicus Open Access hub	https://scihub.copernicus.eu/
4	Bathymetry	Bathymetry	1	0.0625 degrees	-	Raster (.png)	EMODnet	https://www.emodnet-bathymetry.eu/
5	Seabed Slope	Seabed Slope	1	0.0625 degrees	-	Raster (.png)	EMODnet	https://www.emodnet-bathymetry.eu/
6	River Discharge	River Discharge data	3	Hourly step - time series	1981 to 2010	ASCII (.csv)	SMHI HYPEWeb	https://hypeweb.smhi.se
7	Land Cover	Corine 2018	1		2018	Vector (.shp)	Copernicus Land Monitoring Service	https://land.copernicus.eu/pan-european/corine-land-cover/clc2018
8	Seabed Substrate	Seabed Substrate	1	1:1M	-	Vector (.shp)	EMODnet	http://drive.emodnet-geology.eu/geoserver/gtk/wms
9	Geology	GISEurope Bedrock and Structural geology	1	1:1.5M	-	Raster (.png)	OneGeology	http://www.onegeology.org/

Satellite images

Earth Explorer (Landsat 4-5 TM and Landsat 8 OLI)

The Landsat Thematic Mapper (TM) sensor was carried onboard Landsat 4 and 5 from July 1982 to May 2012 with a 16-day repeat cycle, referenced to the Worldwide Reference System-2. Very few images were acquired from November 2011 to May 2012. The satellite began decommissioning activities in January 2013. Landsat 4-5 TM image data files consist of seven spectral bands. The resolution is 30 meters for bands 1 to 7. The Thermal infrared band 6 was collected at 120 meters but was resampled to 30 meters. The approximate scene size is 170 km north-south by 183 km east-west (Table 2).

The Landsat Operational Land Imager (OLI) captures data with improved radiometric precision over a 12-bit dynamic range, improving the overall signal to noise ratio. Landsat 8 launched on February 11, 2013, with a 5-day repeat cycle, referenced to the Worldwide Reference System-2. Providing moderate-resolution imagery, from 15 meters to 100 meters, of Earth's land surface and polar regions, Landsat 8 operates in the visible, near-infrared, short wave infrared, and thermal infrared spectrums. Landsat 8 captures more than 700 scenes a day. The OLI sensor collects image data for 9 shortwave spectral bands over a 190 km swath (Table 3).

Table 2. Landsat 4-5 Thematic Mapper (TM) band list.

Landsat 4-5	Wavelength (micrometres)	Resolution (meters)
Band 1	0.45-0.52	30
Band 2	0.52-0.60	30
Band 3	0.63-0.69	30
Band 4	0.76-0.90	30
Band 5	1.55-1.75	30
Band 6	10.40-12.50	120 (30)
Band 7	2.08-2.35	30

Table 3. Landsat 8 Operational Land Imager (OLI) band list.

Landsat 8	Wavelength (micrometres)	Resolution (meters)
Band 1 (Coastal / Aerosol)	0.433 – 0.453	30
Band 2 (Blue)	0.450 – 0.512	30
Band 3 (Green)	0.525 – 0.600	30
Band 4 (Red)	0.630 – 0.680	30
Band 5 (Near Infrared)	0.845 – 0.885	30
Band 6 (SWIR)	1.560 – 1.660	120 (30)
Band 7 (SWIR)	2.100 – 2.300	30
Band 8 (Panchromatic)	0.500 – 0.680	15
Band 9 (Cirrus)	1.360 – 1.390	30

Sentinel 2 Mission

The Copernicus Sentinel-2 mission comprises a constellation of two polar-orbiting satellites placed in the same sun-synchronous orbit, phased at 180° to each other. It aims at monitoring the variability observed in the land/sea surface conditions. The satellite has high swath width (290 km) and increased revisit time (10 days at the equator with one satellite, and 5 days with 2 satellites, under cloud-free conditions, which results in 2-3 days at mid-latitudes). These characteristics make Sentinel 2 a satellite capable to support the continuous monitoring of Earth's surficial changes. Sentinel-2 satellites are on track from 2016 to today, and the produced image data files consist of twelve spectral bands, with a higher resolution of 10 m (Table 4).

Table 4. Sentinel 2 band list.

Sentinel 2	Central wavelength (micrometres)	Resolution (meters)
Band 1 (coastal aerosol)	0.44	60
Band 2 (Blue)	0.49	10
Band 3 (Green)	0.56	10
Band 4 (Red)	0.66	10
Band 5 (Red Edge 1)	0.70	20
Band 6 (Red Edge 2)	0.74	20
Band 7 (Red Edge 3)	0.78	20
Band 8 (NIR)	0.83	10
Band 8A (NIR Vapor)	0.86	20
Band 9 (Water Vapor)	0.94	60
Band 10 (SWIR-Cirrus)	1.37	60
Band 11 (SWIR-1)	1.61	20
Band 12 (SWIR-2)	2.20	20

Coastal erosion analysis methodology by processing historical satellite images

Satellite image selection

Historical satellite images were retrieved from the satellite imagery repositories covering the period from the early 1980s to late 2020 (Table 5). The historical satellite image selection was mainly based on the correct geo-reference of each image, on the clarity from cloud cover, and the seasonality. All images were retrieved during the summer months (May to September) and in the same tidal phase (ebb tide phase) to minimize the error of the tidal effect.

The shoreline movement analysis was carried out into two different periods, based on the spatial resolution of the examined satellite images:

- a) Five satellite images from Landsat 4-5 TM, covering almost 25-year time period (from 1985 to 2010), were retrieved from the Earth Explorer database, provided by United States Geological Survey Global Visualizer (USGS - <https://earthexplorer.usgs.gov/>).
- b) A satellite image was selected from Landsat 8 OLI collection for 2015. The image was retrieved from the Earth Explorer database, provided by USGS.
- c) Six satellite images from Sentinel 2 sensor, covering a 5-year period (from 2015 to 2020), were retrieved from the Copernicus Open Access Hub, provided by Copernicus and European Space Agency (<https://scihub.copernicus.eu/>).

Table 5. Data product specifications.

Data Products	Number of images retrieved	Resolution	Year of Image Acquisition	Source
Landsat 4-5 TM	6	30 m	1985 to 2010	Earth Explorer, USGS
Landsat 8 OLI	1	5 m	2015	
Sentinel 2	6	3.1 m	2015 to 2020	Copernicus Hub

Table 6 presents the selected satellite images for the coastal erosion assessment in the Greek PONTOS pilot site. All selected images refer to the summer months. Moreover, the images were chosen by the clarity from the cloud cover, the correct geo-reference, and orthorectification. An additional parameter considered was the similarity on the tidal phase (based on data from TPXO 7.2) or the Sea Surface Height (using data from CMEMS).

Table 6. List of the selected Satellite images.

No	Date	Data Products	Resolution	Dataset	Type of file / Format	Index
1	23-08-85	Landsat 4-5 TM	30 m	TM Collection 2 Level-1	.TIF	NDWI
2	19-08-90	Landsat 4-5 TM	30 m	TM Collection 2 Level-1	.TIF	NDWI
3	31-07-95	Landsat 4-5 TM	30 m	TM Collection 2 Level-1	.TIF	NDWI
4	16-08-00	Landsat 4-5 TM	30 m	TM Collection 2 Level-1	.TIF	NDWI
5	29-07-05	Landsat 4-5 TM	30 m	TM Collection 2 Level-1	.TIF	NDWI
6	12-08-10	Landsat 4-5 TM	30 m	TM Collection 2 Level-1	.TIF	NDWI
7	09-07-15	Landsat 8 OLI	30 m	OLI collection Level-1	.TIF	NDWI
9	25-08-15	Sentinel 2B	10 m	Sentinel-2 mission	.TIF	NDWI
10	10-07-16	Sentinel 2B	10 m	Sentinel-2 mission	.TIF	NDWI
11	30-07-17	Sentinel 2B	10 m	Sentinel-2 mission	.TIF	NDWI
12	14-08-18	Sentinel 2B	10 m	Sentinel-2 mission	.TIF	NDWI
13	14-08-19	Sentinel 2B	10 m	Sentinel-2 mission	.TIF	NDWI
14	28-08-20	Sentinel 2B	10 m	Sentinel-2 mission	.TIF	NDWI

Coastline extraction from satellite images

The methodology applied at all PONTOS study areas entails the semi-automatic shoreline delineation procedure. Historic satellite images were processed, and their historical shorelines were extracted using the semi-automatic classification technique, allowing the identification of land and sea areas in an image, based on their spectral signatures.

1. The Normalized Difference Water Index (NDWI), introduced by McFeeters (1996), was utilized for the classification process. The NDWI value is used to produce a binary classification of water vs. non-water areas. As water bodies strongly absorb light in the visible to the infrared electromagnetic spectrum, NDWI uses green and near-infrared bands to highlight water bodies. NDWI was calculated, according to the McFeeters (1996) formula:

$$NDWI = \frac{(\text{Band Green} - \text{Band NIR})}{(\text{Band Green} + \text{Band NIR})}$$

2. The produced NDWI image was imported to the Semi-Automatic Classification Plugin (SCP) for QGIS (Congedo, 2016), and around 30 Regions of Interest

(ROI's) were manually identified on each historical image by training the algorithm into two main macro-classes: *Land* and *Water*. The new raster file was further classified into two bands (*Land* and *Water*) by applying the minimum distance classification algorithm.

3. The shoreline was extracted by vectorizing the classified raster image and then applying a Gaussian filtering algorithm to smooth the produced polyline and receive a better fit to the coast (Figure 2).
4. The exact process was applied for each historical satellite image, and consequently, all historical shorelines were finally extracted.

The **validation** of the semi-automatic classification method and the error assessment was estimated by comparing the shoreline polyline, extracted by the semi-automatic technique, with a very high-resolution satellite image Geo-Eye-1 (<0.5 m spatial resolution).

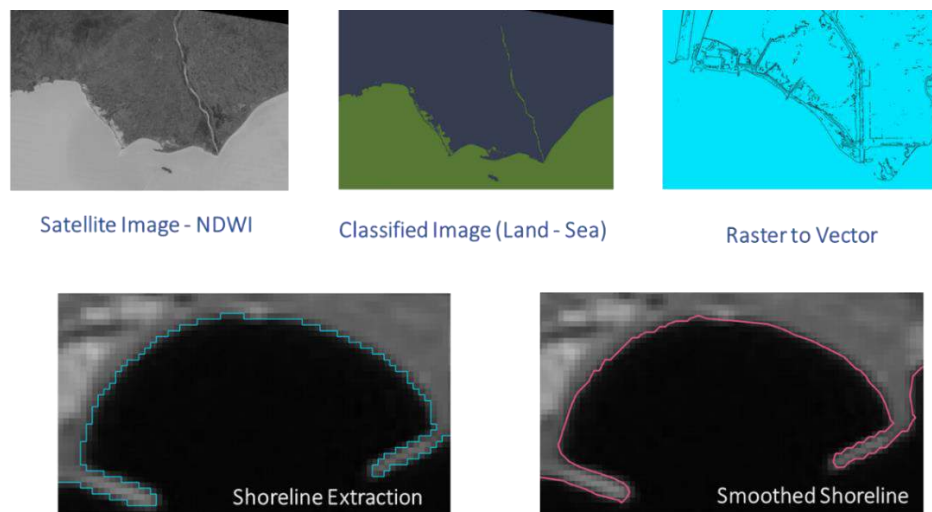


Figure 2. Coastline extraction methodology in steps.

Evaluation of the shoreline evolution

Based on the satellite image resolution, the shoreline analysis was performed for two discrete time periods (1985 – 2015 and 2015 – 2020). The evaluation of the shoreline evolution was performed by the Digital Shoreline Analysis System (DSAS), provided by the USGS (Thieler et al., 2009). The DSAS tool generates vertical to the coastline transects positioned along the shoreline at distances of 20 m. The reference baseline

required by the DSAS tool was manually digitized and set offshore and parallel to the most recent shoreline (2020). A series of statistical indicators were produced, such as:

- a) the Net Shoreline Movement index (NSM, in m), reporting the distance between the oldest and the latest shorelines for each transect,
- b) the End Point Rate (EPR, in m/y), calculated by dividing the distance of Net Shoreline Movement by the time elapsed between the oldest and the latest shoreline, and
- c) the Weighted Linear Regression (WLR, in m/y), in which the weight w is a function of the variance of the measurement uncertainty (Genz et al., 2007):

$$w = 1/e^2 \quad (1)$$

where e is the shoreline uncertainty value.

Using the data produced by the DSAS transects, a statistical analysis of the shoreline evolution along the study years was applied, and various statistical parameters were computed and analyzed. The results were verified by applying two methodologies for outlier removal:

- The Interquartile Range (IQR) method, and
- The method of extreme values removal (based on quantile distribution – 1%) to “clip” the data and remove the outliers.

Both methods were applied in combination with the optical and empirical detection.

Validation of the satellite image classification method

The shoreline extraction methodology was validated using a reference coastline extracted by a higher resolution satellite image. This image is from the GeoEye-1 sensor with spatial resolution 0.46 m in the Panchromatic and 1.84 m in RGB NIR bands. The GeoEye-1 shoreline was used as a reference coastline, since its accuracy is higher than Sentinel 2 and Landsat 8 OLI satellite images (Figure 3).

The GeoEye-1 satellite is equipped with the most advanced technological sensor systems ever used in commercial remote sensing. The satellite collects images at 0.46 m panchromatic (black-and-white) and 1.84 m multispectral resolution. The satellite can collect up to 500,000 sq km of pan-sharpened multispectral imagery per day. This capability is ideal for large-scale mapping projects. GeoEye-1 can revisit any point on Earth once every three days or sooner.



Figure 3. Satellite images (in NDWI) used for the validation process.

The validation method was applied by comparing the shorelines extracted from Landsat 8 OLI (30 m spatial resolution), the Sentinel 2B (10 m spatial resolution), and the GeoEye-1 (1.84 m spatial resolution).

The Sentinel 2B satellite image selected herein was collected at the exact date and time with the GeoEye-1 image. On the other hand, Landsat 8 OLI images obtained at the same date were unavailable, so the closest available date was selected (see Table 7). The satellite images were georeferenced in a similar manner and had almost zero cloud cover. The distance between the shorelines was estimated using vertical transects (at 2 m distance). The distance between the intersect points was evaluated, and the final statistical parameters were produced (Figure 4).

Table 7. Satellite images selected for the methodology validation.

	Landsat 8 OLI	Sentinel 2B	GeoEye1
DATE	19/10/2020	22/10/2020	22/10/2020
Time	08:58	09:10	09:12
Resolution	30	10	0.46, 1.84
Band	G, NIR	G, NIR	Pan, RGB NIR

Wave data

In this section, the offshore and nearshore wave characteristics are analyzed. In the first stage, the offshore wave time series retrieved from CMEMS were statistically analyzed, presenting the average wave direction and the extreme wave events. Then, applying the equations of the Ray-Wave Model, the incident wave energy and the longshore sediment transport were estimated.

- Wave products (significant wave height, wave propagation direction, and wave period) for the period 2015-2020 were retrieved from the CMEMS database, based on the referral points defined above. These wave products are the integrated parameters computed from the total wave spectrum (significant wave height, period, direction, Stokes drift, etc.) produced by the WAM model simulating the wave field over the Mediterranean Sea.
- As shown in Figure 2, the data points selected were located along the coastal zone of the study area. The data retrieval was based on scripts that automatically retrieve data for each of the referral points. Subsequently, further analysis, based on innovative tools that were created for this dataset, was applied.
- More precisely, wave-roses of data for each CMEMS cell were produced, and a Peaks Over Threshold analysis (POT) was applied to estimate the average wave height and the extreme wave values at all CMEMS cells. In addition, wave data were used to calculate the wave characteristics at the nearshore and breaker zone, aiming to compute the longshore Incident Wave Energy.



Figure 5. Discretization of study area according to CMEMS wave time-series dataset. The retrieved data refer to the central point of each coastal grid cell.

Peaks Over Threshold analysis

The Peaks Over Threshold analysis (POT) is a systematic way to analyze the distribution of the exceedances over a specified threshold and to estimate the extreme quantiles outside the range of observed values. The method is based on the observation that the extreme tail of distribution often has a relatively standardized and straightforward form, regardless of the shape at the central parts of the distribution. One then fits such a simple distribution only to those observations that exceed some suitable level, hoping that this fitted distribution gives an accurate fit to a well-known theoretical distribution (e.g., Normal, Log-Normal, Gumbel, Weibull, etc.), at the more extreme parts. The threshold level should be chosen high enough for the tail to have approximately the standardized form, but not so high to allow a few observations above it. After fitting the appropriate tail distribution, one estimates the distribution of the (random) number of exceedances over the level and then combines the tail distribution of the individual exceedances with the distribution for the number of exceedances to find the total tail distribution. Finally, the expected extreme waves per certain return period is assessed for each grid point.

Expected exceedance

The simplest distribution to fit the exceedances over a level u is the Generalized Pareto distribution, GPD, with distribution as in equation (2). Note that if a random variable X

follows a Generalized Pareto distribution, then the exceedances over a level u also follow the GPD distribution function, with the same k -parameter but with different scale parameter.

$$P(X > u + y | X > u) = \frac{\left(1 - k \frac{u + y}{\sigma}\right)^{1/k}}{\left(1 - k \frac{u}{\sigma}\right)^{1/k}} = \left(1 - k \frac{y}{\sigma - ku}\right)^{1/k} \quad (2)$$

Another important property of the Generalized Pareto Distribution is that if $X > u$, then the mean exceedance over this level u is a linear function of u :

$$E(X - u | X > u) = \frac{\sigma - ku}{1 + k} \quad (3)$$

Plotting the mean exceedance as a function of u can help us decide on a proper threshold value. The resulting plot is called Mean Residual Life plot, also referred to as mean excess plots in the statistical literature.

Poisson + GPD = GEV

If one successfully fits a Generalized Pareto distribution to the tail of data, one would like to use the GPD to predict the extreme values that might occur over a certain period. One could, for example, want to predict the most extreme wave heights that will appear during a year or with a return period of 25, 50 or 100 years. If the distribution of the individual significant wave height exceedances is GPD, one can easily find, e.g., the distribution of the largest value of a fixed number of exceedances. However, the number of exceedances is not fixed but random, and then one has to combine the distribution of the random size of individual exceedances with the random number of exceedances N , before expressing anything about the total maximum. If the level u is high, we can assume N to have an approximate Poisson distribution, due to the Poisson approximation of the Binomial distribution and neglect the dependence of nearby values. Now, there is a nice relationship between the Generalized Pareto distribution and the Generalized Extreme Value distribution in this respect: the maximum of a Poisson distributed number of independent GPD variables has a GEV distribution. This follows by simple summation of

probabilities: if N is a Poisson distributed random variable with mean μ , and is the maximum of N independent GPD variables then,

$$\begin{aligned}
 P(M_N \leq x) &= \sum_{n=0}^{\infty} P(N = n) \cdot P(X_1 \leq x, X_2 \leq x, \dots, X_n \leq x) \\
 &= \sum_{n=0}^{\infty} e^{-\mu} \frac{\mu^n}{n!} \cdot \left(1 - \left(1 - k \frac{x}{\sigma} \right)^{1/k} \right)^n \\
 &= \exp \left\{ -\left(1 - k(x - a) / b \right)^{1/k} \right\}
 \end{aligned} \tag{4}$$

which is the Generalized Extreme Value distribution with and.

This means that we can estimate the distribution of the maximum significant wave height during the winter months (December – February) based on the historical CMEMS dataset, by fitting a GPD to the exceedances over some level u , estimating μ by the number of exceedances N divided by the number of months ($7 \times 3 \times 2 = 42$) and use the above relation to fit a GEV distribution.

Declustering

The POT method relies on two properties of peaks over the selected threshold: they should occur randomly in time according to an approximate Poisson process, and the exceedances should have an approximate GPD distribution and be approximately independent. In practice, one does not always find a Poisson distribution for the number of exceedances. Since extreme values sometimes have a tendency to cluster, a declustering algorithm should be applied, to identify the largest value in each of the clusters, and then use a Poisson distribution for the number of clusters. The selected peaks should be sufficiently far apart for the exceedances to be independent.

To select the clusters and check the Poisson character one can use the dispersion index, which is the ratio between the variance and the expectation of the number of peaks. For a Poisson distribution this ratio is equal to one. An acceptable peak separation should give a dispersion index near one.

Wave Characteristics at the Nearshore and Breaker Zone and Incident Wave Energy Calculation

Retrieved wave data from the CMEMS database were comprised of the daily time-series of the spectral significant wave height (H_{m0}), the zero up-crossing wave period (T_{M10}), and the wave propagation direction, relative to the North (ϕ_o). These data were imported into a simple wave-ray model, as open sea significant wave height (H_o), wave period (T) and open sea direction (ϕ_o), to transform the offshore wave characteristics into the wave characteristics at the nearshore and breaker zone:

Wave data were comprised of the daily time-series of:

- I. the spectral significant wave height (H_{m0}),
- II. the zero up-crossing wave period (T_{02}), and
- III. the wave direction relative to the north (ϕ_o).

These data, as open sea significant wave height (H_o), wave period (T), and the wave propagation direction (ϕ_o), were imported into a simple one-dimensional wave-ray model to transform the offshore wave characteristics into the wave characteristics at the breaker zone.

More precisely, a long list of parameters was estimated, such as:

- I. the **wavelength** [m],
- II. the **wave celerity** [m/s],
- III. the **wave group celerity** [m/s],
- IV. the **breaker zone width and depth** [m],
- V. the **significant wave height** at the breaker [m],
- VI. the **shoaling coefficient**, K_S ,
- VII. the **refraction coefficient**, K_R ,
- VIII. the **wave dispersion coefficients** at offshore and breaker zones, n_o and n_{BR} ,
- IX. the **wave direction** at the breaker zone, ϕ_{BR} [°],
- X. the **longshore wave-induced current**, V_{long} [m/s],
- XI. the **incident wave energy** at the breaker zone, E_{BR} [$J\ m^{-1}\ s^{-1}$],
- XII. the **longshore sediment transport** on an annual basis, Q_L [$m^3\ yr^{-1}$].

All parameters were produced following the equations described by the Coastal Engineering Manual (2008), as presented in **Σφάλμα! Το αρχείο προέλευσης της αναφοράς δεν βρέθηκε..**

Therefore, the estimated longshore sediment transport at each coastline segment was directly correlated to the assessed shoreline change rates, over the study periods.

Table 9. Wave characteristics at the nearshore zone using the offshore CMEMS wave data.

Wave Characteristics	Units	Equation	Equation
Deep-sea wavelength	[m]	$\lambda_o = \frac{gT^2}{2\pi}$	(5)
Deep-sea wave celerity	[m/s]	$C_o = \frac{\lambda_o}{T}$	(6)
Deep-sea group wave celerity	[m/s]	$C_{g,o} = \frac{C_o}{2}$	(7)
Deep-sea wave dispersion coefficient		$n_o = \frac{1}{2} \left(1 + \frac{2kh}{\sinh(2kh)} \right)$	(8)
Breaker zone wave length	[m]	$\lambda_b = \sqrt{\tanh\left(\frac{4\pi^2 h_b}{gT^2}\right)}$	(9)
Breaker zone wave celerity	[m/s]	$C_b = \sqrt{gh_b}$	(10)
Breaker zone group wave celerity	[m/s]	$C_{g,b} = n_b C_b$	(11)
Breaker zone significant wave height	[m]	$H_b = H_o \times K_s \times K_R$	(12)
Shoaling coefficient		$K_s = \sqrt{\frac{C_o}{2n_b C_b}}$	(13)
Refraction coefficient		$K_R = \sqrt{\frac{\cos 2\phi_o}{\cos \phi}}$	(14)
Breaker zone wave dispersion coefficient		$n_b = \frac{1}{2} \left(1 + \frac{2k_b h_b}{\sinh(2k_b h_b)} \right)$	(15)
Breaker zone wave direction	[°]	$\phi_b = \sqrt{\frac{n_o \lambda_o}{n \lambda_b}}$	(16)
Wave breaker zone depth	[m]	$h_b = H_b / \gamma$	(17)
Longshore current speed	[m/s]	$V_{long} = 20.7 m \sqrt{gH_b} \sin(2\phi)$	(18)
Incident wave energy at the breaker zone	J/(m s)	$P = \frac{\rho g}{16} H_b^2 C_{g,b} \sin(2\phi)$	(19)
Longshore sediment transport	m ³ /yr	$Q_{long} = 3.6 \times 10^6 H_b^{5/2} \sin(\phi)$	(20)

Where $\gamma = 0.78$ is the breaker index, and m is the bottom slope at the breaker zone, derived from bathymetric maps.

Study Site Description

The Greek Pilot area is located in the coastal zone on both sides of the Nestos River. Nestos river is a transboundary river springs in Rila Mountains in central Bulgaria, crosses the terrain of Bulgaria, enters Greece, and discharges into the Thracian Sea in Northern Greece (long, lat: 24.8038, 40.8469). The river basin is 5,479 km² in total (approximately 2,000 km² in Greece), while its length is 243 km, of which 130 km are in Greek territory. The river forms a significant ecosystem throughout its course and discharges in its Delta, where a floodplain is formed covering 440 km². Coastal and riparian wetlands form a unique natural ecosystem protected by the Ramsar Convention (Boskidis et al., 2011). The coastal zone's total length is estimated at around 50 km, covering the coastline from Vassova lagoon (in the Gulf of Kavala) to Avdira port (East boundary, (long, lat) = (24.5430°E,40.9556°N); West boundary, (long, lat) = (24.9670°E,40.9336°N). Along the western part of the coastline, a complex system of lagoons (Vassova, Eratino and Agiasma lagoons) is situated; to the center, the Keramoti gulf and the west Nestos river bank, and to the east, the eastern Nestos river bank and two of the most touristic beaches in Thrace (Maggana and Myrodato). The coastline continuation is interrupted by several irrigation channels, and many streams outflow to the open sea. Moreover, the five lagoons and the Nestos river runoff transfer fresh water and sediments to the coastal zone (Sylaios et al., 2005).

The entire coastal zone is characterized by intense erosion due to the operation of three hydroelectric and irrigation dams along the course of the Nestos River. Their construction began in the early 1960s, and they were completed by the end of 1996, resulting in a gradual disturbance in the erosion–deposition balance, especially at the vicinity of the deltaic zone (Sylaios et al., 2012). Andreadaki et al. (2008) estimated a sediment supply reduction in relation to historical sediment yields at the deltaic zone of 84 %, due to Nestos river damming. Nestos River presently supplies the coastal zone with fresh water, having a total annual runoff ranging between 600×10^6 and 800×10^6 m³, with limited seasonal variability (Sylaios et al., 2012). Plume water shows a limited hydrographic signature in the form of local, shallow, freshwater lenses covering the first surface meter of the water column throughout the year (Kamidis et al., 2011).

To study efficiently the shoreline evolution at the broad Nestos River deltaic area, the study site was divided into four sub-areas, according to their geomorphological characteristics and shoreline orientation (Table 10).

Table 10. Table of the sub-areas' boundaries.

Sub-Areas	Study site coordinates		Coastline length	Orientation	Sediment type
	East (Long, Lat)	West (Long, Lat)			
Vassova - Agiasma Beach	24.5430,40.9556	24.6265,40.8614	13.3 km	SW	sand-mud
Gulf of Keramoti	24.6265,40.8595	24.7010,40.8596	7.5 km	S	sand
Keramoti Beach - West Nestos	24.6864,40.8585	24.8028,40.8461	11 km	S	sand
East Nestos - Avdira Port	24.8056,40.8477	24.9670,40.9336	17 km	SE	sand

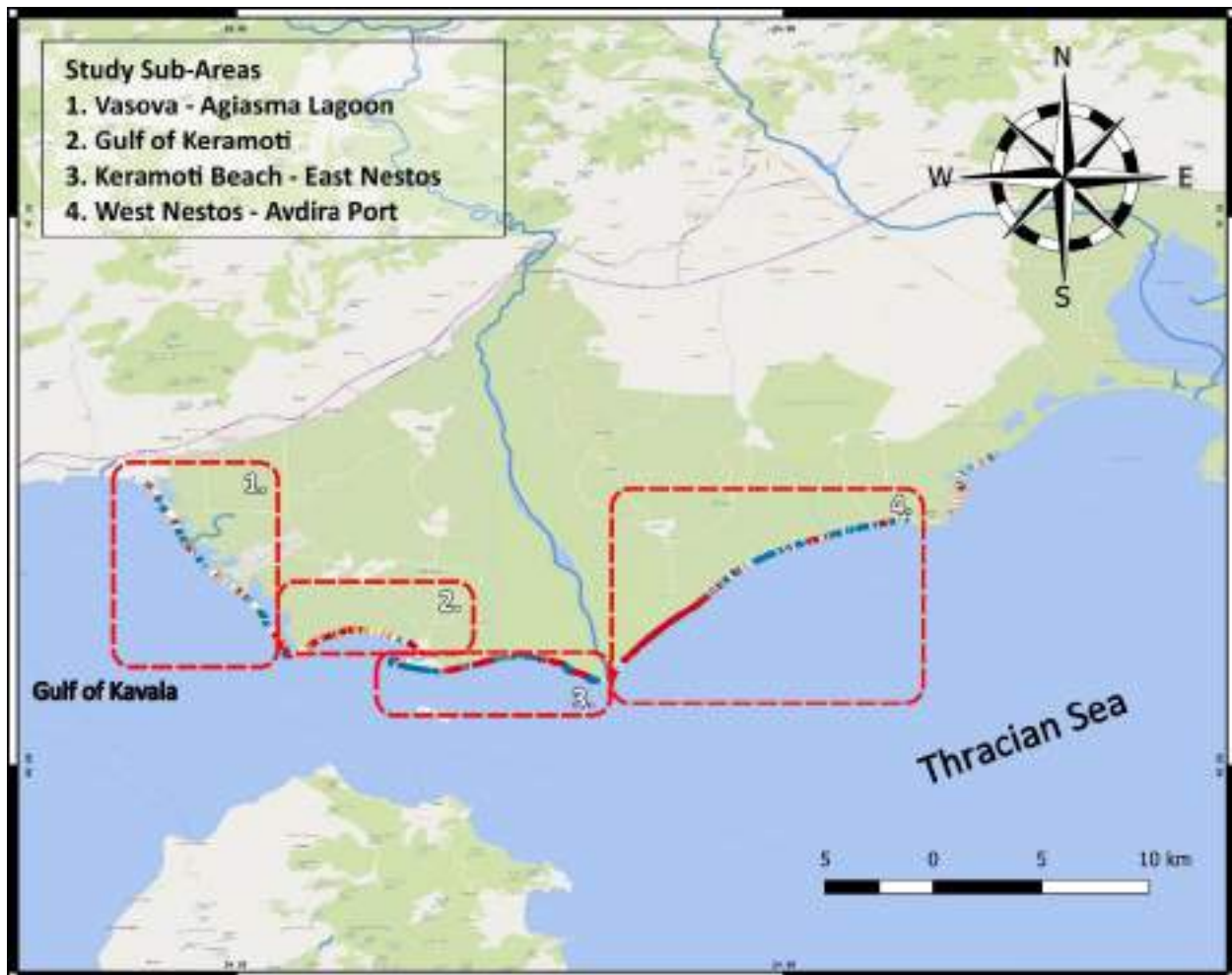


Figure 6. Sub-areas as divided along the study area.

Geomorphology and Bathymetry

The sedimentary basin of the Nestos River delta constitutes part of the broader quaternary basin of Prinos, including the Nestos delta and the sea between Thassos island and the mainland around Kavala Gulf. The Prinos-Nestos basin is also part of the broader tectonic basin of the south Rhodope Range. Therefore, the basin's bedrock

consists of Rhodope mass rocks (gneisses, schists, amphibolites, marbles, etc.) (Figure. 7). Due to the basin's continuous subsidence, the thickness of its deposits ranges approximately from 2.5 to 6.0 km (Psilovikos, et al., 1988). The initial faulting and subsidence of South Rhodope are located in the Lower to Middle Miocene (Lalechos et al., 1977; Proedrou, 1979). The deeper layers of the basin's deposits consist of conglomerates and sandstones deposited in a pre-delta environment. During the Upper Miocene, intense evaporation and the deposition of evaporates and clastic sediments followed in alternative layers. Later, during Pliocene and Pleistocene, sedimentation turned again to clastic materials with the deposition of sandstones, mudstones and claystones into the marine-deltaic environment (Lalechos et al., 1977). The Quaternary and recent deposits of the Nestos basin delta are not more than one to two hundred meters thick and consist of gravels, sands, silts and clays in a lensial and alternating (cyclothem) pattern, deposited principally in a deltaic environment. The modern soils of the coastal zone consist of sands, silts and clays in various proportions. The relief of the coastal zone under discussion is low to almost level. The beach consists of coarse to fine sand and its width varies from 10 m up to 50 m in some places. The beach sands are extended seawards forming a zone of 300 to 400 m of shallow waters, (less than 10 m deep), surrounding the coastline. This shallow water zone is extended up to 900 m at some places, e.g., at Ammoglossa (Cape Akroneri) and at the river Nestos mouth. This means that at least some of the sediments extracted from coastal erosion and/or discharged by the river Nestos waters are deposited nearshore and along the western coastal zone of the delta.

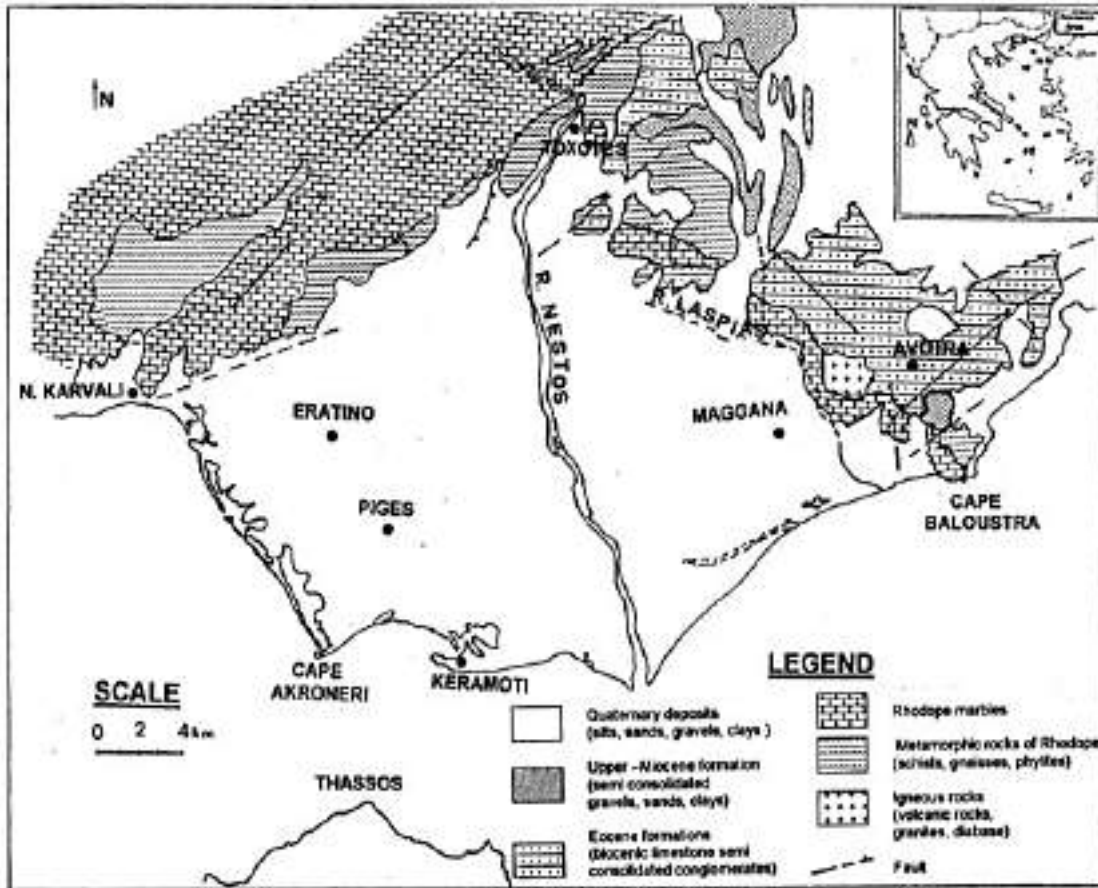


Figure 7. Geological map of Nestos River delta study area.

Figure 8 shows the coastal zone bathymetry, characterized by small depths in the breaking zone (under 50 m). The seafloor is sloping gradually at most parts of the area, especially along the continental coastline, presenting zones with shallow depths near the lagoon system due to the transport of river-borne sands. These deposits and the entire area's sediments are formed mostly by fine sands near the coastline, gradually replaced by silts, as bathymetry increases until the maximum depth of approximately 25 m. The thickness of the surface sediment layer in the coastal zone varies between 10 and 50 m, increasing from the western part of the strait toward the deltaic area (Conispoliatis and Lykousis 1986).

These sediments form relict sand deposits having similar geotechnical characteristics to the sediments of presently eroded Keramoti beach. Stratigraphic examination in the area was limited; however, two 20 m deep boreholes indicate a sequence of silty sands, fine silty sands, and sandy silts. Sedimentary succession also presents the absence of coarse-grained layers, i.e., gravels and pebbles, deposited near the sea bottom surface.

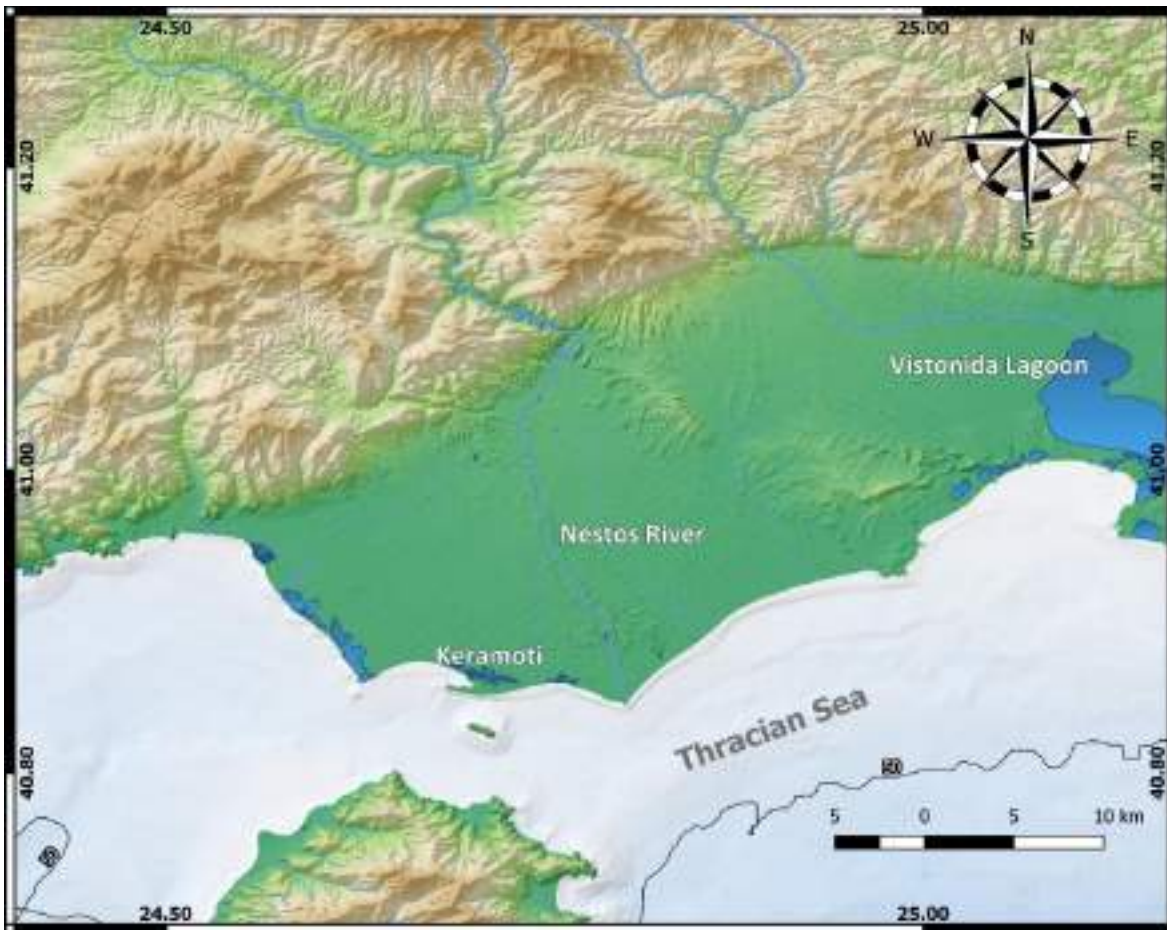


Figure 8. Bathymetric map of Nestos study site

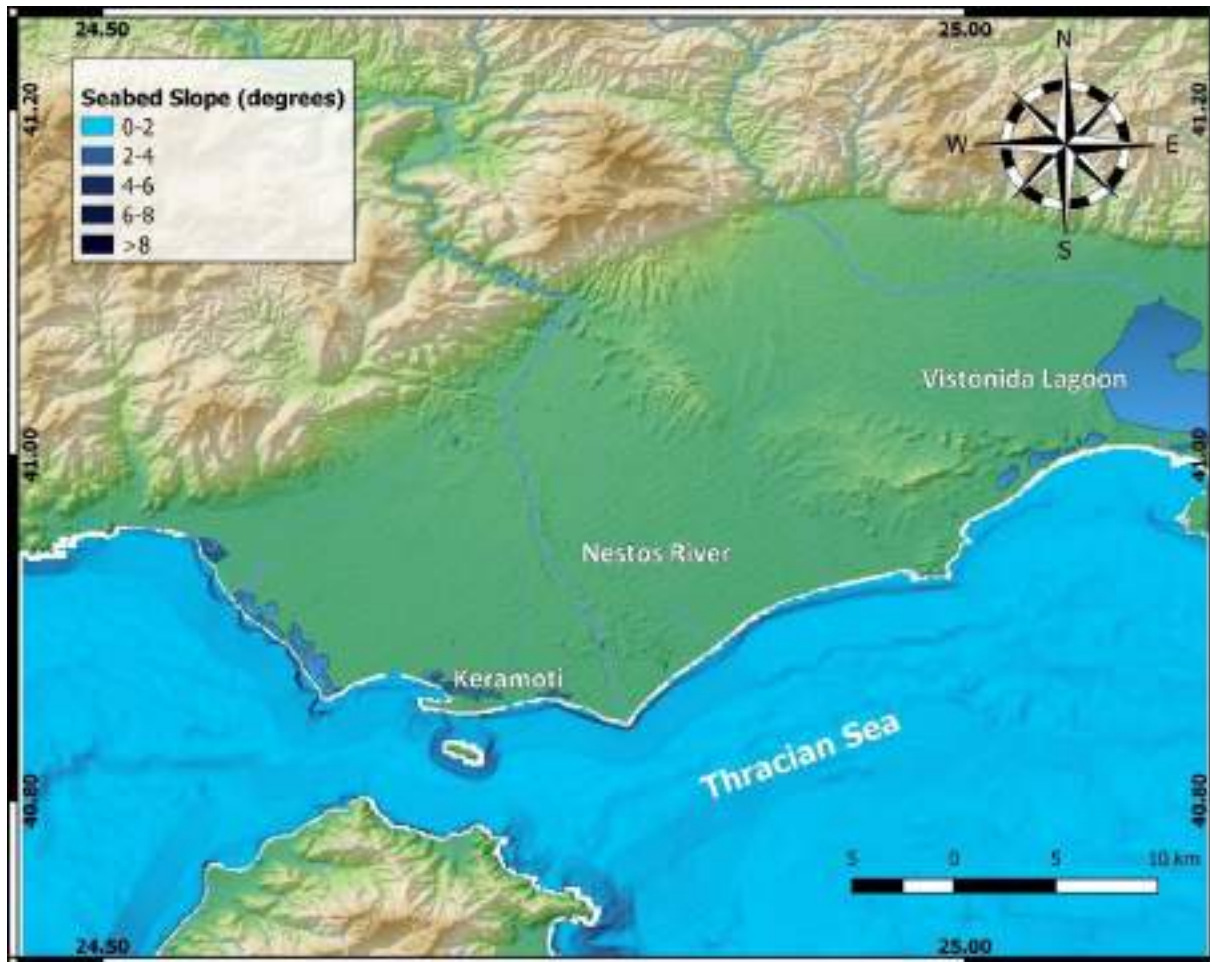


Figure 9. Bottom slopes in Nestos study site.

Land Cover Data

The more significant part (82%) of the Nestos River basin is mountainous and is covered by natural vegetation (41% is covered with forests). Agricultural areas cover 17% of the basin, and the urban regions merely 1% of the river basin. Agricultural and animal farming activities occur near Paranesti, Stavroupoli, and Paschalia, the main villages in the area, but no intense human activities generally occur.

Figure 10 shows the Nestos river plain's land cover (data retrieved from the CORINE Land Cover, 2018). The coastal zone consists of long sandy beaches with fine grain sediment, orientated from the Nestos river outflow and the complex coastal lagoon system. Moreover, salt and inland marshes are reported. Along the western coastline, a long sandy beach with a complex lagoon system is observed. In the Gulf of Keramoti,

long muddy salt marshes and agricultural land (Vineyards) are reported. Additionally, the coastal zone of western and eastern of Nestos delta consisted of sandy beaches and sand marshes.

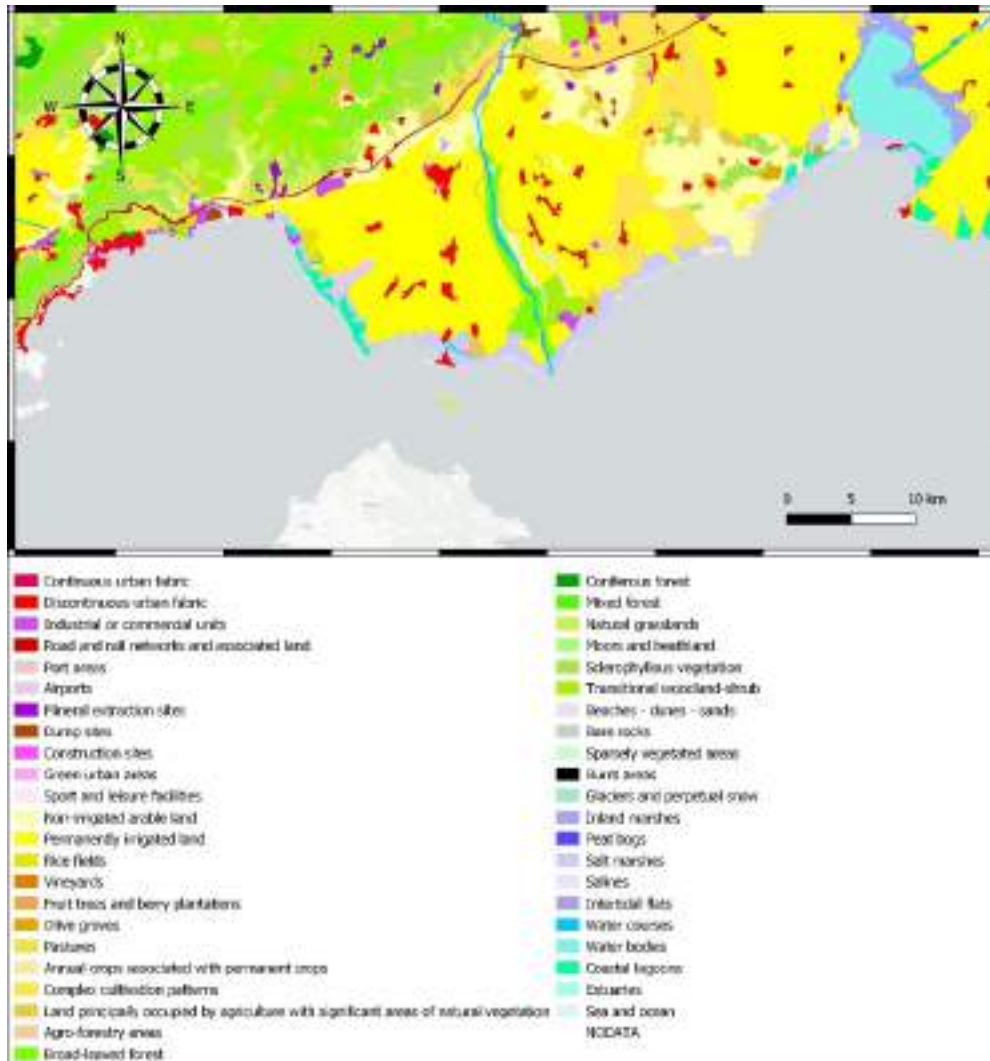


Figure 10. Land cover map of the Nestos Study site.

River Discharge Data

Nestos river presents the lower discharge rates among the other rivers outflow in Thracian Sea. The outflow of the Nestos river, as recorded in the period 1981-2010, is shown in Figure 11. A clear downward trend is observed during the period 1981-1993. On the contrary, during the period 1993-2010, there is a significant upward trend that occurs mainly after 2002 as the annual runoff exceeds the average annual runoff of the whole period in almost all years. The maximum flow occurred in 1997 with a runoff of

$1,499.619 \times 10^6 \text{ m}^3/\text{y}$. This is due to an extreme event that happened in the first days of May of the same year. Another considerable high freshwater occurred in 2010 with a runoff of $1,424.820 \times 10^6 \text{ m}^3/\text{y}$, while the minimum in 1993 with $506.707 \times 10^6 \text{ m}^3/\text{y}$. It is noteworthy that after 1993 the average monthly flow reached almost $16 \text{ m}^3/\text{s}$. The maximum flow occurred in the winter months up to May, while in the summer months up to September, the runoff regulated by the dams maintains an almost constant value of about $23 \text{ m}^3/\text{s}$.

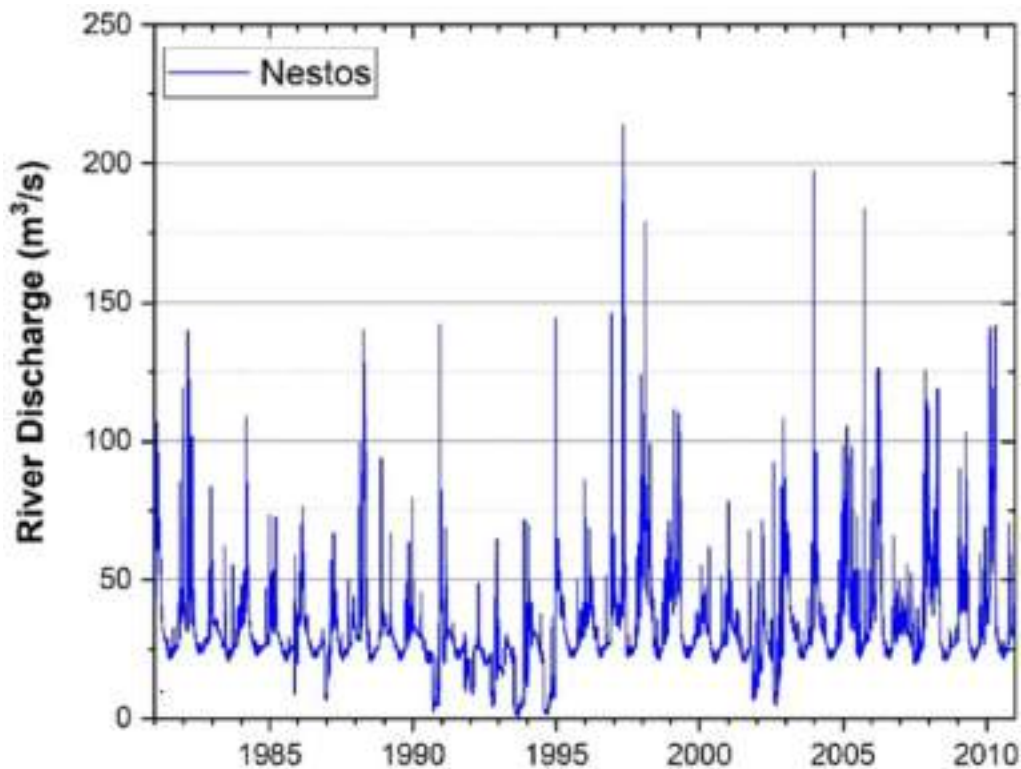


Figure 11. Temporal variability of daily discharge of Nestos river (retrieved from HYPE database).

Wave analysis

Wave time series analysis

Historical offshore wave time-series data at sixteen points along the coastline (in hourly time-step) were retrieved from the reanalysis product of the Copernicus Marine Environmental Monitoring Service (CMEMS) covering the period 2015-2019 and from the forecast product of the CMEMS covering the period 2019-2020. The parameters retrieved were VHM0 (spectral significant wave height), VMDR (Wave direction), VTM10 (zero up-crossing wave period). Figure 12 shows the CMEMS points along the coastline.



Figure 12. CMEMS points and their codes along the study area.

Analyzing the time-series we find that the prevailing wave direction at the western part of the coastline is S-SE (direction from which waves propagate), with a mean offshore significant wave height of ~ 0.2 m and maximum at 1.4 m. Since the orientation of the western coastline is NW-SE, the waves move almost parallel to the coastline. In the narrow straight between Thassos Island and Keramoti, the waves are mainly orientated from the west; the average height is ~ 0.3 m, and the maximum wave height is approximately 1.6 m. The sandy beaches at the western bank of the river mouth receive waves from S-SE direction, with an average height of about 0.4 m and maximum about 2.7 m. Finally, the beaches at the eastern bank of Nestos River receive waves propagating from S and SE directions, with average height of about 0.3 m and maximum wave height around 3.0 m (Table 12 and Figure 13).

Table 11. The wave characteristics in the points along the coastline

Point Code	Frequent Wave Direction	Mean Significant Wave Height	Max Significant Wave Height
177008	S	0.1	1.3
166436	S	0.2	1.4
176437	S-SE	0.1	1.4
175662	S-SE	0.2	1.5
175863	E	0.3	1.5
175864	E	0.3	1.6
175865	E	0.3	1.8
175866	E-SE	0.3	2.2
175867	E-SE	0.4	2.7
175868	S-SE	0.4	2.9
175869	S-SE	0.4	3.0
176438	S-SE	0.3	2.9
176439	S-SE	0.3	3.0
176440	S-SE	0.3	3.1

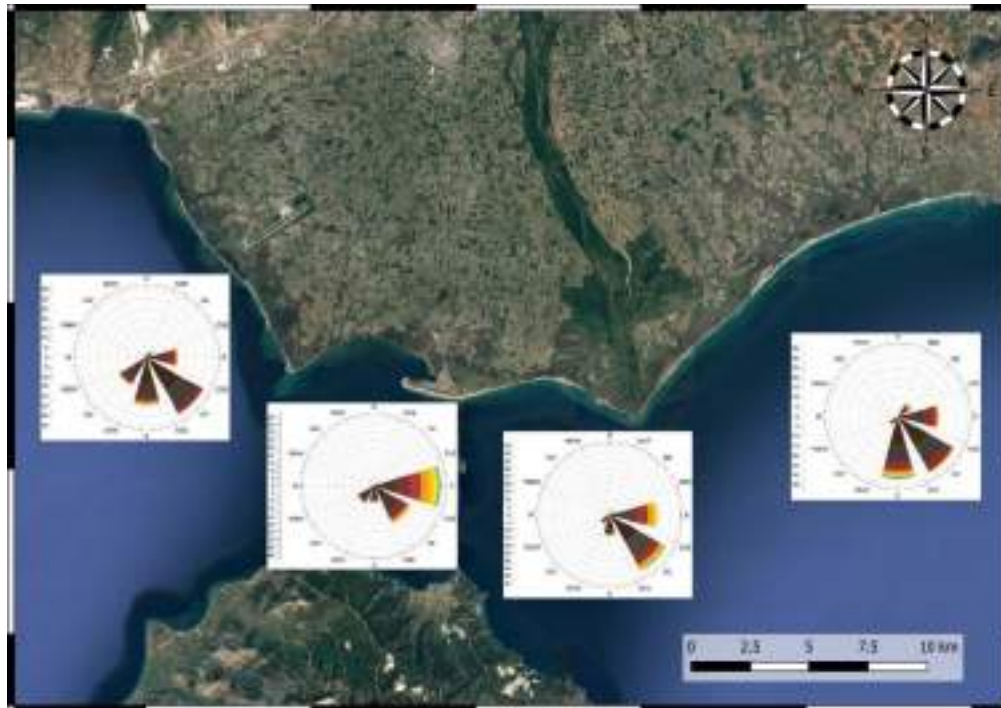


Figure 13. The wave direction at four indicative sites along the study coastline.

Results of CMEMS extreme Wave data analysis

In the following Table, results from the extreme wave data analysis are presented.

Table 12. Results from the statistical analysis on the CMEMS data to derive the Extreme Wave Events at the offshore points along the coastline.

Point	Date	Threshold	Frequency	mean	min	max	Point	Date	Threshold	Frequency	mean	min	max
177008	2014-2015	0.5	10	0.8	0.5	1.3	175866	2014-2015	1.0	10	1.4	1.1	2.2
	2015-2016	0.5	7	0.7	0.5	1.1		2015-2016	1.0	7	1.4	1.1	1.7
	2016-2017	0.5	6	0.8	0.6	1.3		2016-2017	1.0	4	1.5	1.1	1.9
	2017-2018	0.5	5	0.6	0.5	0.6		2017-2018	1.0	9	1.2	1.1	1.4
	2018-2019	0.5	8	0.6	0.5	1.0		2018-2019	1.0	10	1.2	1.0	1.6
	2019-2020	0.5	7	0.6	0.5	0.8		2019-2020	1.0	5	1.2	1.0	1.4
176436	2014-2015	0.6	9	0.9	0.7	1.4	175867	2014-2015	1.2	8	1.8	1.2	2.7
	2015-2016	0.6	5	0.9	0.8	1.2		2015-2016	1.2	7	1.8	1.2	2.2
	2016-2017	0.6	6	0.9	0.7	1.4		2016-2017	1.2	6	1.7	1.2	2.5
	2017-2018	0.6	9	0.7	0.6	0.8		2017-2018	1.2	8	1.4	1.2	1.8
	2018-2019	0.6	8	0.8	0.6	1.1		2018-2019	1.2	10	1.5	1.2	1.9
	2019-2020	0.6	7	0.7	0.6	0.8		2019-2020	1.2	5	1.5	1.2	1.9
176437	2014-2015	0.5	12	0.7	0.5	1.4	175868	2014-2015	1.3	7	1.9	1.4	2.9
	2015-2016	0.5	5	0.8	0.7	1.1		2015-2016	1.3	7	1.9	1.3	2.4
	2016-2017	0.5	6	0.9	0.6	1.3		2016-2017	1.3	6	1.9	1.3	2.7
	2017-2018	0.5	7	0.6	0.5	0.6		2017-2018	1.3	7	1.5	1.3	1.9
	2018-2019	0.5	7	0.7	0.5	1.0		2018-2019	1.3	10	1.6	1.3	2.0
	2019-2020	0.5	7	0.6	0.5	0.7		2019-2020	1.3	6	1.6	1.3	2.1
175862	2014-2015	0.8	9	1.1	0.9	1.5	175869	2014-2015	1.3	8	1.9	1.3	3.0
	2015-2016	0.8	6	1.0	0.9	1.1		2015-2016	1.3	7	2.0	1.3	2.5
	2016-2017	0.8	7	1.0	0.8	1.4		2016-2017	1.3	6	1.9	1.4	2.8
	2017-2018	0.8	8	1.0	0.9	1.2		2017-2018	1.3	7	1.6	1.4	2.0
	2018-2019	0.8	10	1.0	0.8	1.2		2018-2019	1.3	9	1.6	1.4	2.1
	2019-2020	0.8	6	0.9	0.8	1.0		2019-2020	1.3	6	1.7	1.4	2.2
175863	2014-2015	0.8	9	1.1	0.9	1.5	176438	2014-2015	1.2	8	1.8	1.2	2.9
	2015-2016	0.8	7	1.0	0.8	1.1		2015-2016	1.2	9	1.7	1.2	2.4
	2016-2017	0.8	7	1.0	0.8	1.3		2016-2017	1.2	5	2.0	1.3	2.7
	2017-2018	0.8	9	1.0	0.8	1.2		2017-2018	1.2	5	1.5	1.2	1.9
	2018-2019	0.8	11	1.0	0.8	1.3		2018-2019	1.2	9	1.5	1.3	1.9
	2019-2020	0.8	4	0.9	0.9	0.9		2019-2020	1.2	7	1.5	1.2	2.1
175864	2014-2015	0.9	9	1.2	0.9	1.6	176439	2014-2015	1.3	6	2.1	1.4	3.0
	2015-2016	0.9	7	1.1	1.0	1.2		2015-2016	1.3	8	1.9	1.3	2.5
	2016-2017	0.9	7	1.1	0.9	1.4		2016-2017	1.3	5	2.0	1.4	2.8
	2017-2018	0.9	8	1.1	0.9	1.2		2017-2018	1.3	5	1.6	1.3	2.0

	2018-2019	0.9	12	1.0	0.9	1.3		2018-2019	1.3	9	1.6	1.3	2.1
	2019-2020	0.9	4	0.9	0.9	0.9		2019-2020	1.3	7	1.6	1.3	2.1
175865	2014-2015	0.9	10	1.2	0.9	1.8	176440	2014-2015	1.3	6	2.1	1.4	3.1
	2015-2016	0.9	7	1.2	1.0	1.4		2015-2016	1.3	8	1.9	1.4	2.5
	2016-2017	0.9	7	1.1	1.0	1.6		2016-2017	1.3	7	1.9	1.3	2.9
	2017-2018	0.9	10	1.1	0.9	1.2		2017-2018	1.3	4	1.7	1.6	2.0
	2018-2019	0.9	9	1.1	0.9	1.4		2018-2019	1.3	7	1.7	1.4	2.2
	2019-2020	0.9	3	1.0	0.9	1.1		2019-2020	1.3	8	1.6	1.4	2.2

Based on the Extreme Wave Analysis, at the eastern offshore sites of the study site (points 175868, 175869, 176438, 176439, and 176440) highest wave activity has taken place, with the most frequent wave directions from S and SE. The mean wave height varies from 0.3 to 0.4 m, and under extreme storm events the wave height reaches up to 3.1 m. The frequency of the extreme wave events is over 6 events per year, with the 2017-2018 the less energetic period reported (only 4 to 5 events). The most energetic period was 2018-2019, with an average of 9 storm events and waves exceeding 3 m in height (Figure 14).

Along the straight between Keramoti and Thasos Island (points 175863, 175864, 175865, 175866, and 175867), the wave activity is significantly lower compared to that recorded at the eastern coast. In that region, the mean wave height varies from 0.3 to 0.4 m, and waves propagate mainly from the E direction at the deeper parts of the Keramoti Gulf. Their direction changes to S and SE at the offshore of western Nestos bank. In Keramoti, the annual extreme wave events frequency varies from 12 (in 2018-2019) to 3 (in 2019-2020), exhibiting mean wave height of 1.1 m and maximum of 1.5 m. Additionally, at the western coastal zone of Nestos River, the annual extreme wave events frequency varies from 10 (in 2018-2019) to 5 (in 2019-2020), showing mean significant wave height of 1.6 m and maximum of 2.5 m (Figure 14).

The wave activity is significantly lower at the western offshore area (points 177008, 166436, 176437, and 175662). In that region, the mean wave height is around 0.2 m, and the waves propagate mainly from S and SE directions. Even under extreme weather conditions, the wave height appears below 1.5 m, with the maximum value being recorded at the south of the Agiasma lagoon. According to the extreme wave analysis, waves exceeding 0.6 m are considered extreme events, and the average frequency of occurrence varies from 6 to 10 events per year (Figure 14).

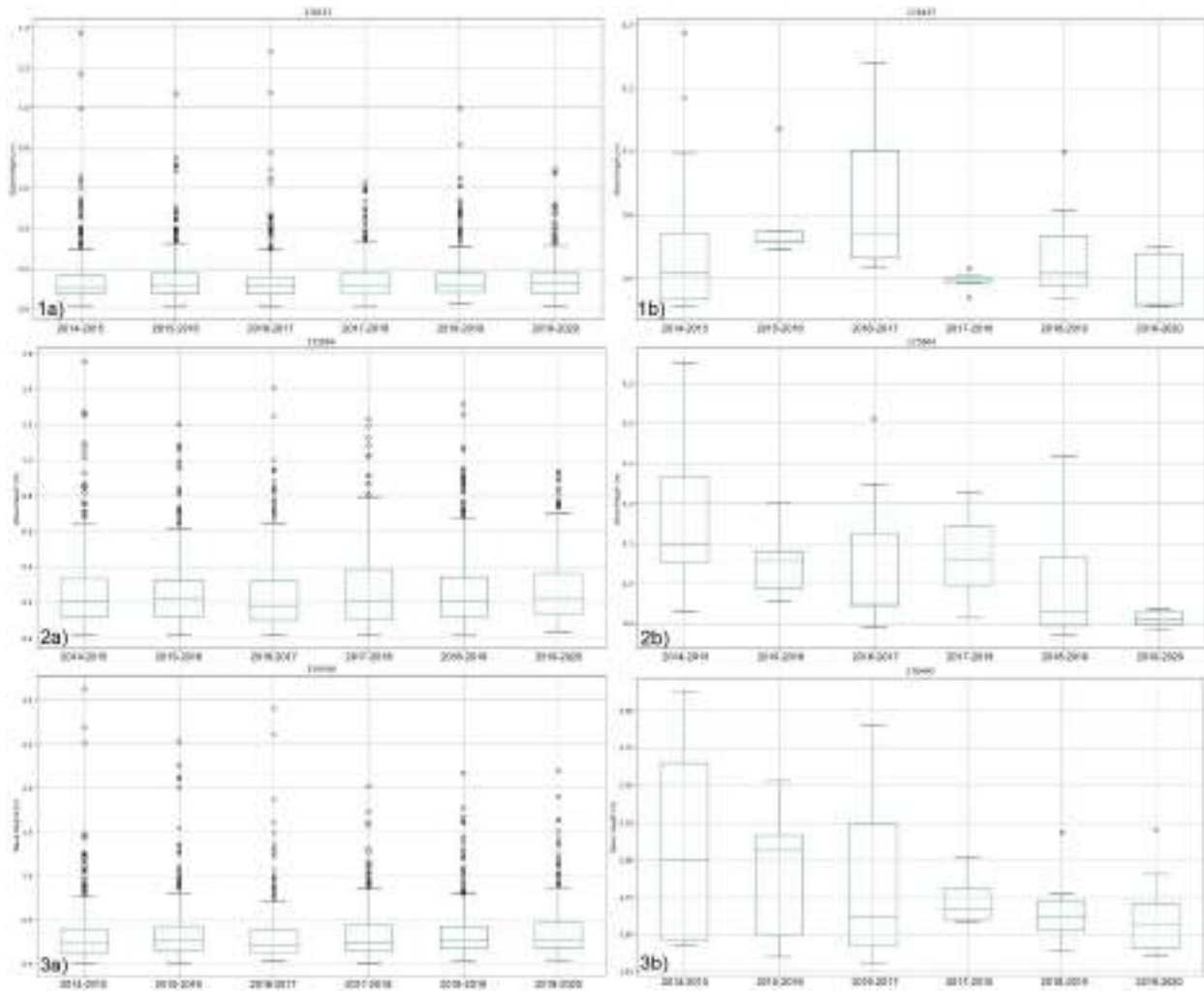


Figure 14. CMEMS wave data analysis at the western (1a and 1b), central (2a and 2b), and eastern (3a and 3b) offshore points. Left panels present the annual Box-Whisker plots of the significant wave heights. The extreme wave events are shown with black dots. Right panels present the boxplots of the Extreme Wave Events.

The Ray-Wave Model

The incident wave energy influences the sediment budget and affects sediment transport according to the wave height and direction. Such patterns possibly determine the accretion/erosion hotspots observed at the shoreline. The negative sign indicates the sediment transport from West to East and the positive from East to West. The most frequent wave orientation along the western coastline occurs from SE, with average wave height around 0.3 m and average annual incident wave energy to the breaker zone approximately at $13.6 \text{ J m}^{-1}\text{s}^{-1}$. This wave energy is capable to transfer in the along-shore direction around 63.4 m^3 sediment per year from the south-east towards the north-west beaches of the study area. The mean magnitude of the longshore current speed is 0.1

m/s. At the sandy beaches of Keramoti and western Nestos estuaries, waves propagating from E direction dominate. The average incident wave energy is estimated at $28.5 \text{ m}^{-1}\text{s}^{-1}$ and approximately 146.2 m^3 sand is transferred annually from the eastern coast towards the west. The average current speed is about 0.05 m/s. The incident wave energy increases eastwards, since the coast receives S and SE waves with an average height of about 0.3 m. The incident wave energy reaches up to $382.75 \text{ J m}^{-1}\text{s}^{-1}$ and the sediment moves from west to east with an average current speed of about 0.2 m/s. The eastern coastal zone is exposed to extreme wave events, since waves exceeding 3 m have been recorded.

Table 13. The Ray Wave Model results in three indicative areas of the study site

	Period	Annual incident wave energy ($\text{J m}^{-1}\text{s}^{-1}$)	Annual Theoretical Sediment Longshore flux (m^3/yr)	Wave Induced Longshore Current (m/s)
West	2020-2019	-9.26	-41.9	-0.06
	2019-2018	-1.79	-4.52	-0.04
	2018-2017	-31.33	-151.2	-0.1
	2017-2016	-2.12	-6.93	-0.06
	2016-2015	-23.48	-112.5	-0.09
Central	2020-2019	-31.2	-159.9	-0.04
	2019-2018	-51.6	-264.1	-0.05
	2018-2017	-5.7	-34.36	-0.017
	2017-2016	-41.1	-211.2	-0.02
	2016-2015	-11.6	-61.32	-0.005
East	2020-2019	59.78	301.33	0.241
	2019-2018	74.88	382.75	0.228
	2018-2017	3.08	18.77	0.166
	2017-2016	65.24	332.56	0.205
	2016-2015	31.33	159.8	0.172

Results from the Coastal Erosion Analysis

The methodology applied to assess and define the coastal erosion activity and identify the coastal erosion “hotspots” along the coastal zone of Nestos River delta was based on the shoreline movement analysis, by processing historic satellite images, using remote sensing techniques and GIS software. The analysis was applied in two time periods (1985-2015 and 2015-2020), analyzing historical satellite products (Landsat and Sentinel imagery) with a different spatial resolution (30 and 10 m, respectively).

- a) The **first shoreline movement analysis covers a 30 years period (1985 to 2015)** using 5-year time step. For this analysis, satellite images from Landsat 4-5 TM and Landsat 8 OSI collection databases were used. The spatial resolution of the satellite image bands for Green and NIR is 30 m. Images were retrieved from the Earth Explorer database (USGS).
- b) **The more recent analysis covers the period 2015 to 2020** (in annual time step), using satellite images from the Sentinel 2 collection, with 10 m spatial resolution in bands Green and NIR. The satellite images were retrieved from the Copernicus Open Access Hub or the Planet Explorer database.

The results of the coastal erosion analysis are presented according to the geographical sub-areas:

1. West study site (Vassova lagoon – Agiasma lagoon)
2. Gulf of Keramoti
3. East coastline of Nestos estuaries
4. West coastline of Nestos estuaries

The statistical parameters presented in Figure 15 designating the shoreline movement are:

- a) The **Shoreline Change Envelope (SCE)**. The parameter represents the greatest distance among all the shorelines that intersect a given transect (units are in meters).
- b) The **Net Shoreline Movement (NSM)**. The parameter represents the distance between the oldest and the youngest shorelines for each transect (units are in meters).
- c) The **Weighted Linear Regression (WLR)**. In a weighted linear regression, the more reliable data based on satellite image resolution receive greater emphasis and weight, towards determining the best-fit line. In the computation of the rate-of-change statistics for shorelines, greater emphasis is placed on data points for which the position uncertainty is smaller (units are in meters/year).

Additionally, the **estimation of the land change** (in km²), in all sub-areas, by the time elapsed between the oldest and the latest shoreline was assessed and presented in the following sections.

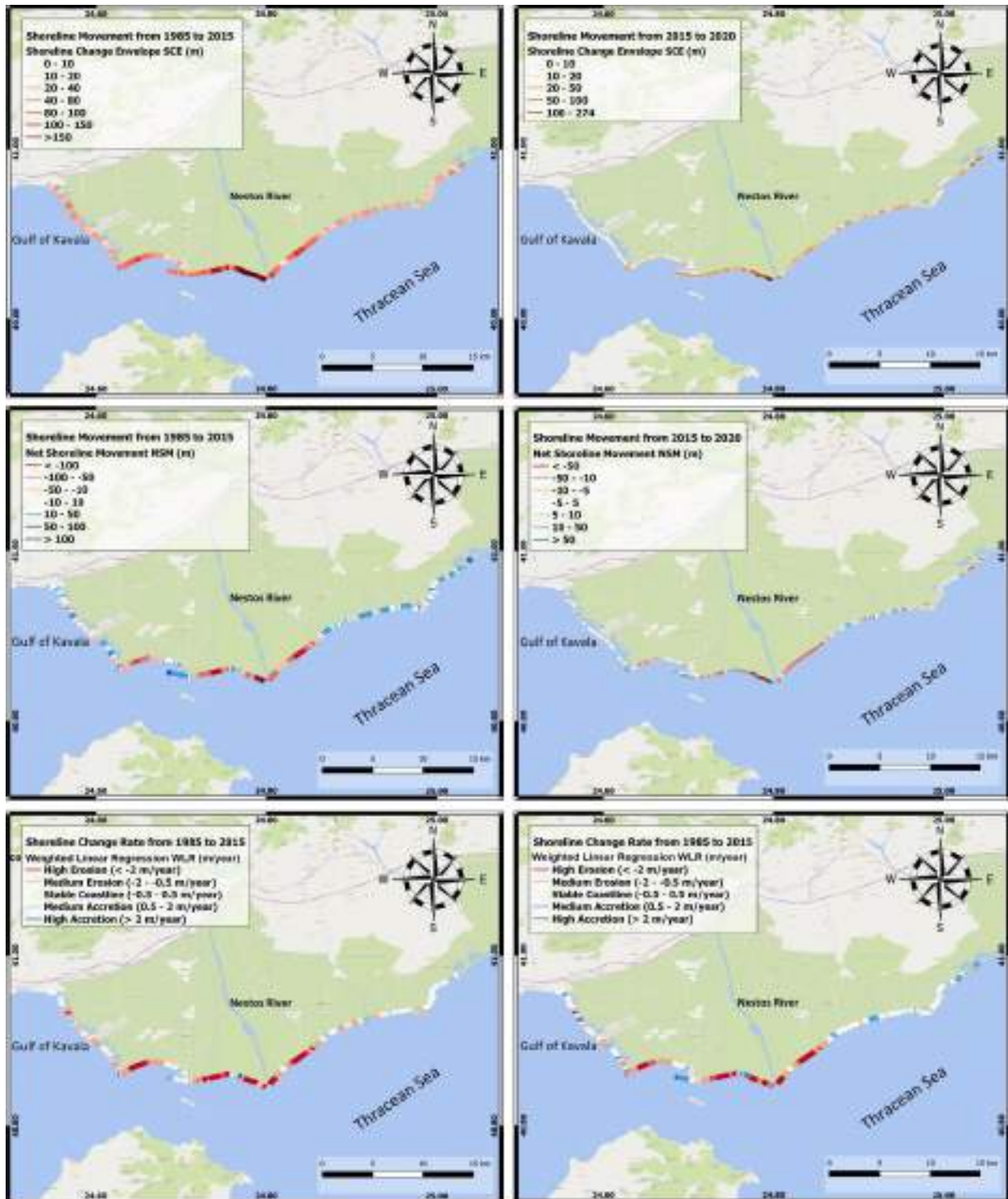


Figure 15. Statistical parameters (SCE, NSM, and WLR) estimated; a) for the period 1985 to 2015 (left column), and b) for the period 2015 to 2020 (right column).

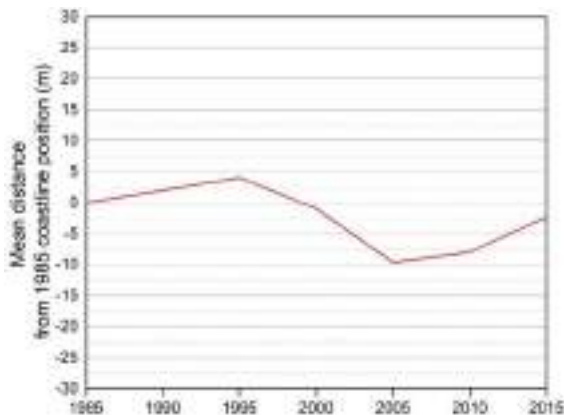
Western Study Area (from Vassova lagoon to Agiasma Beach)

The first sub-area of interest covers the western coastline of the Greek study site, having total length of almost 13 km and SW orientation. This area covers the eastern coast of Kavala's Gulf. It is characterized by a complex lagoonal system (Vasova, Eratino, and Agiasma lagoons) connected to the open sea with more than five canals. Fine-grain sediment is transferred from the inner lagoons to the adjacent shoreline through these canals. The only residential coastal area is the village of Agiasma, located between Eratino and Agiasma lagoon. Overall, significant changes in the shoreline position are observed throughout the years, especially at the shorelines close to the lagoons' exchange canals. More precisely:

1985-2015

The statistic parameters describing the shoreline change from 1985 to 2015 were estimated based on 435 transects positioned perpendicular to the coastline. Figure 16 shows the average coastline change of the total sub-area from 1985 to 2015 using a five-year time increment. More precisely, from 1985 to 1995 slight accretion (approximately 0.4 ± 0.1 m/year) is observed, but over the next decade (1995 to 2005), high erosion rates (up to 1.7 ± 0.1 m/year) were reported. Moreover, during the third decade (2005-2015) the coastline recovers almost to its initial position, characterized by average accretion rate of 1.1 ± 0.1 m/year (Table 14). Overall, significant fluctuation at the shoreline position through the examined years is observed. This western sub-area is characterized as "slightly eroded", since the difference at the average position of the oldest (1985) and the more recent (2015) shoreline is around -2.3 m.

Table 14. Table of the mean shoreline change rate in periods.



Class/time frame	No of Transects	Mean (m/year)	Std. Error
2010-2015	435	1.1	0.1
2005-2010	435	0.3	0.1
2000-2005	435	-1.7	0.1
1995-2000	435	-1.0	0.1
1985-1995	435	0.4	0.1

Figure 16. Temporal variability of the average shoreline position over the period 1985-2015.

Table 15 presents the average, minimum and maximum values of the main statistical parameters (SCE, NSM, and WLR) calculated by the perpendicular to the shoreline transects. The average shoreline change (SCE) estimate at the sub-area is about 26.9 m. The sandy beach between Vassova and Eratino Lagoons exhibits the higher SCE (about 74.8 m), presenting the highest erosion rates (up to -2.8 m/year). Significantly high erosion rates are also observed at the southern channel of the Eratino lagoon (around -1.2 m/year) and the beach located at the sandbar of the Agiasma lagoon (around -1.0 m/year). At both sites, the shoreline has retreated approximately 30-35 m from 1985 to 2015. On the other hand, four accretion hotspots are reported, with the higher rates observed at the outer beach of Eratino lagoon (up to 2.1 m/year) and the beach close to the southern canal of the Agiasma lagoon (up to 1.8 m/year) (Figure 18).

Table 15. Table with the main statistical coastal erosion parameters for the Western Study site (from Vassova lagoon to Agiasma Beach).

	SCE	NSM	WLR
Average	26.9	-2.3	-0.3
Min value	4.2	-74.8	-2.8
Max value	74.8	68.2	2.1

Throughout the examined 30 years period, around 0.233 km² of the coastal zone has been changed, approximately -0.125 km² of land has retreated, and almost 0.108 km² has been accumulated. Significant land loss is observed at the sandy beach between Vassova and Eratino lagoons (~ -0.045 km²), at the beach located to the south of Eratino lagoon (~ -0.3 km²), and at the sandbar of Agiasma lagoon (~ -0.025 km²). On the other hand, the area with the higher sand accumulation is the sandbar of Eratino lagoon (0.024 km²) (Table 16).

Table 16. Table with the erosion and accretion areas at the Western Study site (from Vassova lagoon to Agiasma Beach).

	Area in km ²
Net Area Movement	0.233
Erosion	-0.125
Accretion	0.108
Average	-0.001
Max accretion	0.028
Max erosion	-0.045

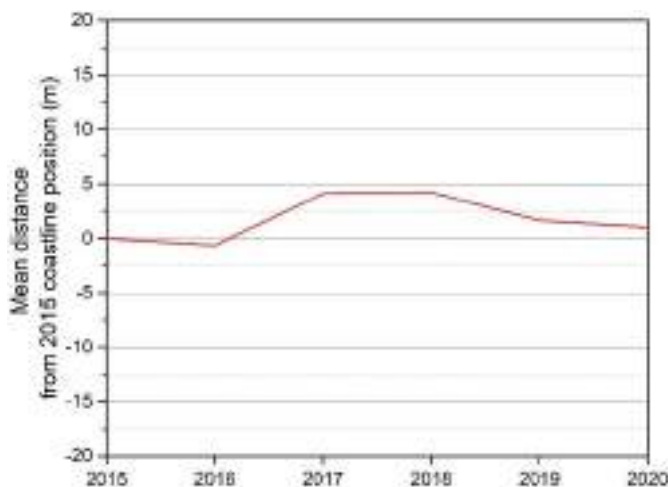
Focusing on the areas of economic interest:

- a) At the Agiasma beach, significant accretion is reported. The coastline overall increased by 10-20 m, with an average rate of around 0.60 m/year. The higher accretion rates are observed to the western part (the part of the beach closer to the canal), with accretion rates up to 0.60 m/year.
- b) It is also important to note that sediment accumulation is reported at most coasts attached to the lagoons' canals. This phenomenon is observed at the Vassova and Agiasma canals. The movement of sediments affects the water quality of both lagoons, increasing the water renewal time of the lagoon.

2015-2020

The statistical parameters describing the shoreline change from 2015 to 2020 were estimated using 638 transects perpendicular to the coastline. Figure 17 illustrates the variability in the annual mean shoreline position of the western coastal zone from 2015 to 2020. Results show that from 2015 to 2016 slight erosion (approximately 0.7 m) is reported. However, during the following year (2016 - 2017), high accretion (up to 4.8 ± 0.1 m/year) is observed. Moreover, from 2018 to 2020, the coastline retreated significantly (up to -2.6 m/year) (Table 17). Overall, slight variation in the shoreline position through the years is observed. The total sub-area is characterized as “slightly accreted”, since the average coastline position moved by only 3 m within the 2015 to 2020 period.

Table 17. Table of the mean shoreline change rate in periods.



Class/time frame	No of Transects	Mean (m/year)	Std. Error
2019-2020	638	-0.6	0.1
2018-2019	638	-2.6	0.1
2017-2018	638	0.1	0.1
2016-2017	638	4.8	0.1
2015-2016	638	-0.7	0.1

Figure 17. Temporal variability of the average shoreline position over the period 2015-2020.

Several erosion or accretion hotspots along the coastal zone for the period 2015 – 2020 are observed. The average shoreline change (SCE) is about 8.9 m, with an average NSM of about 1 m and an average erosion rate of about 0.3 m/year. More precisely, the

higher erosion rates are observed at the sandy beach adjacent to Vassova's Lagoon canal (about -5.6 m/year), where the estimated shoreline movement was ~ 35.3 m. Additional coastal erosion hotspots are observed:

- a) at the northern coastline of Eratino lagoon (WLR= ~1 m/year, NSM= -7 m),
- b) at the coast between Vassova and Eratino lagoons (WLR= ~2.5 m/year, NSM= 10 m),
- c) at the beach located at the Erasmio lagoon sandbar (WLR= ~0.8 m/year, NSM= 7 m), and
- d) at the beach located at the Agiasma lagoon sandbar (WLR= ~2 m/year, NSM= 10 m).

On the other hand, many accretion hotspots are observed along the studied coastline, with the higher accretion rates detected at the sandbar beach of Eratino lagoon (up to 5.8 m/year) and at the beach close to the southern canal of the Agiasma lagoon (up to 5 m/year) (Figure 19).

Table 18. Table with the main statistical parameters for the Western Study site (from Vassova lagoon to Agiasma Beach).

	SCE	NSM	WLR
Average	8.9	1.0	0.3
Min value	0.1	-35.3	-5.6
Max value	35.7	29.7	5.8

Within this five-year period (2015-2020), around 0.071 km² of coastal zone has been altered due to coastal processes. More specifically, approximately -0.028 km² of land has been retreated and 0.043 km² has been accreted. Significant land loss is observed at the beach between Vassova and Eratino lagoons (around -0.045 km²), at the beach located to the south of Eratino lagoon (around -0.3 km²), and at the beach of Agiasma lagoon sandbar (around -0.004 km²). On the other hand, the area with the higher sand accumulation is at the seaside close to the southern canal of the Agiasma lagoon (0.017 km²).

Table 19. Table with the erosion and accretion areas in West Study site (Vassova lagoon - Agiasma Beach).

	Area in km ²
Net Area Movement	0.071
Erosion	-0.028
Accretion	0.043

Average	0.000
Max accretion	0.006
Max erosion	-0.004

The sediment budget in the area seems mainly affected by the canals exchanging water between the open sea and the coastal lagoons and secondary from the Nestos river discharge. The longshore wave currents transfer approximately 64 m³ of sediment per year from SE to NW direction. The total coastline receives the lowest incident wave energy, lower than 13 J m⁻¹s⁻¹, and this makes the coastline rather stable through the years, with limited accretion and erosion hotspots (Table 20).

Table 20. Table of erosion and Ray Wave model results for the west study site

Period	Erosion (m/yr)	Annual incident wave energy (J m ⁻¹ s ⁻¹)	Annual Theoretical Sediment Longshore flux (m ³ /yr)	Wave Induced Longshore Current (m/s)
2020-2019	-0.6	-9.26	-41.9	-0.06
2019-2018	-2.6	-1.79	-4.52	-0.04
2018-2017	0.1	-31.33	-151.2	-0.1
2017-2016	4.8	-2.12	-6.93	-0.06
2016-2015	-0.7	-23.48	-112.5	-0.09

Focusing on the areas of economic interest:

- a) At the Agiasma beach, significant accretion is reported. The coastline moved 3-6 m seawards, with an accretion rate of around 1 m/year. In contrast with the period 1985-2015, the higher accretion rates occurred at the center of the beach, with rates up to 1.3 m/year.
- b) For the period 2015-2020, the phenomenon of sediment accumulation at the coast attached to the lagoons' canals is dominant for Vasova, Eratino, and Agiasma. The sediment accumulation close to the lagoon canal could affect the lagoon's water quality by minimizing the water exchanged between the lagoon and the open sea and increasing the water renewal time.

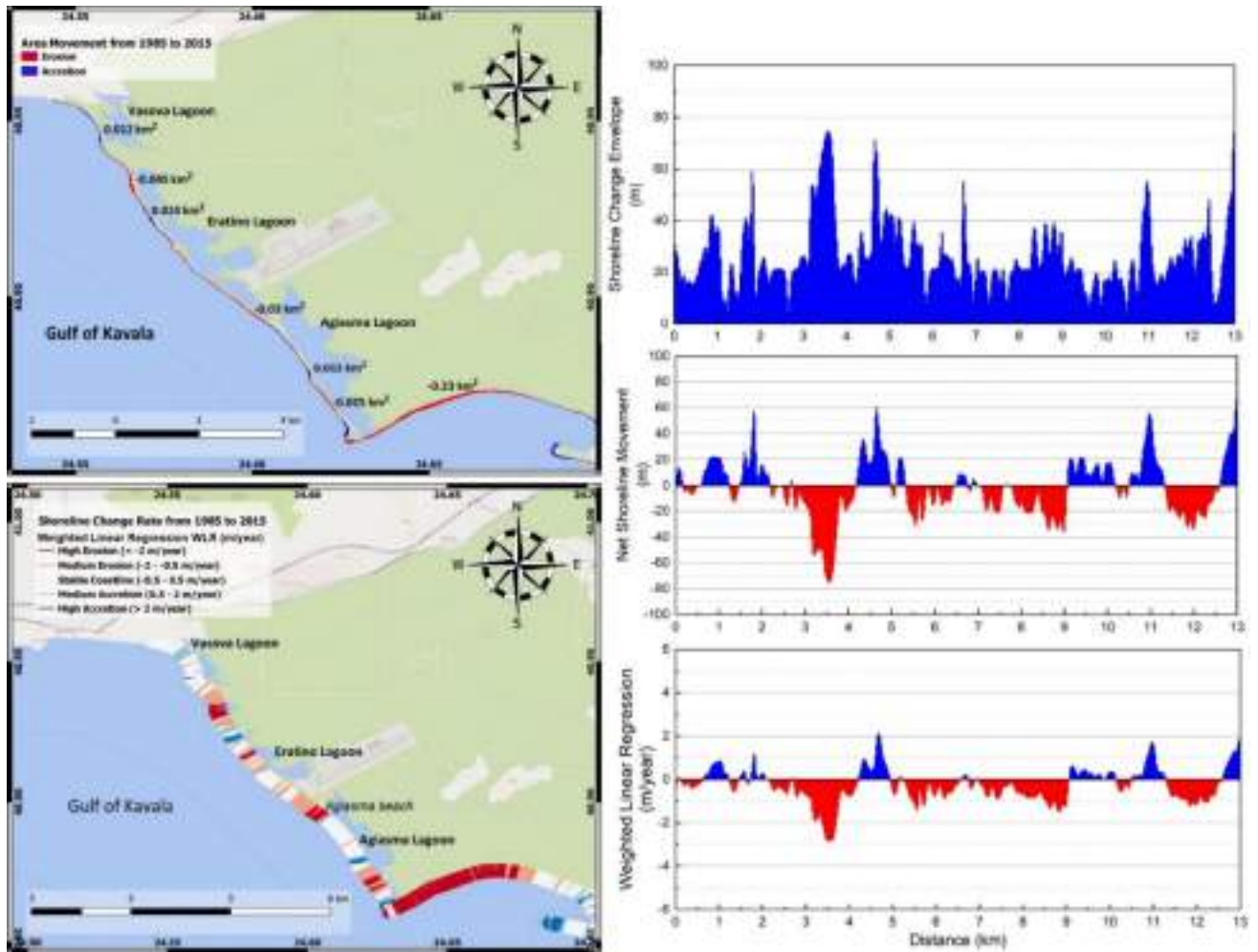


Figure 18. Shoreline evolution from 1985 to 2015. Left panels: a) Map of coastal areal change, and b) Map of the estimated annual shoreline change (WLR). Right panels: The estimated statistical parameters (SCE, NSM, and WLR) per transect along the Western Study coastline.

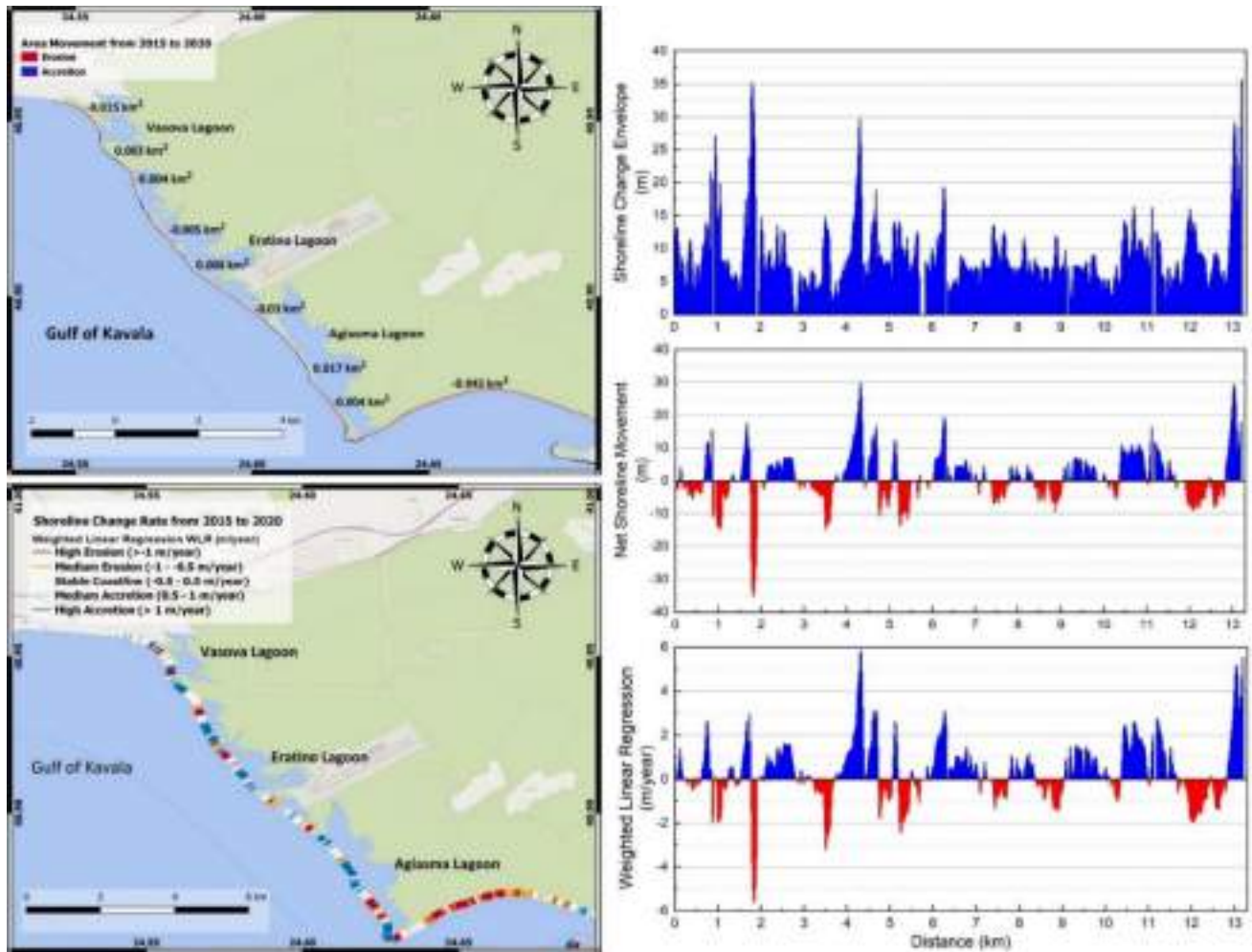


Figure 19. Shoreline evolution from 2015 to 2020. Left panels: a) Map of coastal area change, and b) Map of the estimated annual shoreline change (WLR). Right panels: The estimated statistical parameters (SCE, NSM, and WLR) per transect along the Western Study coastline.

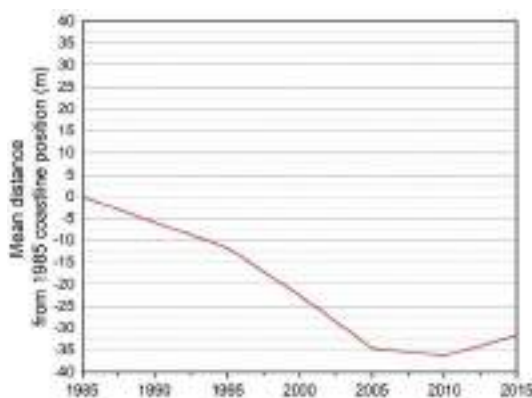
Keramoti Gulf

The coastal area of Keramoti Gulf is the second sub-area of interest. The Gulf has total length of almost 7 km and South orientation. This sub-area, covers the shoreline from Agiasma lagoon to the port of Keramoti. It is a long sandy beach close to salt marshes, wetlands and agricultural land. To the west end of the gulf, the Keramoti village is located. Several drainage canals are located at the central and eastern site of this sandy coastline, outflowing fresh water into Keramoti Gulf. In dry seasons, the water discharge of these canals diminishes to near zero values. To the east end of the gulf is situated the Keramoti lagoon, an internal basin exchanging water and fine grain sediment with the open sea through more than four inlets. Major changes in the shoreline are observed over the study years. Overall, chronic gradual erosion is noted from 1985 to 2020. More precisely:

1985-2015

The statistical parameters representing shoreline evolution in this sub-area from 1985 to 2015 were estimated using 234 coastline transects, located perpendicularly along the shoreline. Figure 20 illustrates the mean shoreline change of the total coastal zone, from 1985 to 2015, using five-year time step. More specifically, from 1985 to 2005, the coastline seems to suffer from acute erosion (up to -2.2 ± 0.1 m/year), since the average position of the shoreline retreats by nearly 35 m. In the next five years (2005 - 2010), the coastline retreats at a lower rate (around -0.3 ± 0.1 m/year), and finally, in the 2010 – 2015 period, slight accretion (about 0.9 ± 0.1 m/year) is observed (Table 21). Overall, the coastline of Keramoti Gulf appears to suffer from gradual erosion, since in this 30-year period, the total shoreline retreated by 32 m.

Table 21. Table of the mean shoreline change rate in periods.



Class/time frame	No of Transects	Mean (m/year)	Std. Error
2010-2015	234	0.9	0.1
2005-2010	234	-0.3	0.1
2000-2005	234	-2.4	0.1
1995-2000	234	-2.2	0.2
1985-1995	234	-1.2	0.1

Figure 20. Temporal variability of the average shoreline position over the period 1985-2015.

Table 22 presents the average, minimum and maximum values of the main statistical parameters (SCE, NSM, and WLR) calculated using the perpendicular to the shoreline

transects. The average shoreline change (SCE) is around 43.5 m, the average Net Shoreline Movement (NSM) about 31.7 m, and the average erosion rate (WLR) approximates 1.2 m/year. The long sandy beach at the western part of the Gulf depicts the higher erosion activity (SCE= 170.2 m, NSM= 103.5 m, WLR= -3.5 m/year). Accretion hotspots are identified at the Gulf's east end and, more precisely, at the shorelines in the vicinity of drainage canals and lagoon inlets. The land accumulated advances the coast by approximately 30 m, and the accretion rate is estimated between 0.5 and 1.5 m/year.

Table 22. Table with the main statistical parameters for the Gulf of Keramoti.

	SCE	NSM	WLR
Average	43.5	-31.7	-1.2
Min value	3.8	-103.5	-3.5
Max value	170.2	50.8	1.5

Throughout the examined 30-year period, around 0.272 km² of coastal zone has been changed. Almost 95% of the total land appears being retreated (-0.259 km²) while only 5% is accreted (0.014 km²). The most significant land loss is observed at the western coast of the Gulf (around -0.23 km²). On the other hand, the area with the higher sand accumulation is located towards the eastern end of the gulf (0.008 km²) (Table 23).

Table 23. Table with the erosion and accretion areas in the Gulf of Keramoti site.

	Area in km ²
Net Area Movement	0.272
Erosion	-0.259
Accretion	0.014
Average	-0.012
Max accretion	0.008
Max erosion	-0.232

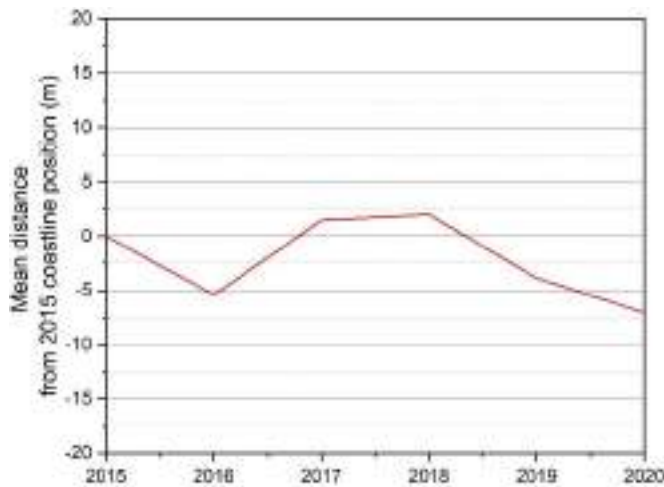
Focusing on the areas of economic interest we may summarize that:

- a) Coastal erosion dominates in the entire coastline over the 2015-2020 period. The shoreline retreats gradually and an extended area of land is lost.
- b) The only area that exhibiting accretion is coast in which the Keramoti shipyard is located, with an average net shoreline movement of 40 m.

2015-2020

The statistical parameters used to describe the shoreline change from 2015 to 2020 were based on the results produced by analyzing 343 transects located perpendicularly along the shoreline. Figure 21 shows the annual average shoreline change of the total coastal zone in Keramoti Gulf. More precisely, from 2015 to 2016, the average position of the coastline shows high erosion rates (up to -5.4 ± 0.2 m/year), since the coast retreats around -5 m. In the next two-year period (2016 - 2018), high accretion is recorded (up to 6.8 ± 0.2 m/year), and the shoreline returns almost to its initial position. In the last two years (2018-2020), the shoreline is retreated by up to -5.8 ± 0.2 m/year, and the mean position of the 2020 shoreline is estimated at -7 m from the shoreline position in 2015 (Table 24). Overall, the coast in Keramoti Gulf is a dynamic environment, with high variations throughout the years, being exposed to storm events and thus being vulnerable to coastal erosion, especially at the western part of the Gulf.

Table 24. Table of the mean shoreline change rate in periods.



Class/time frame	No of Transects	Mean (m/year)	Std. Error
2019-2020	343	-3.2	0.2
2018-2019	343	-5.8	0.2
2017-2018	343	0.5	0.2
2016-2017	343	6.8	0.2
2015-2016	343	-5.4	0.2

Figure 21. Temporal variability of the average shoreline position over the period 2015-2020.

Several hotspots of erosion and accretion along the western coastal zone are observed. The average shoreline change (SCE) reaches 11.1 m, characterized by NSM of about -7.7 m and average erosion rate of about -0.8 m/year. More precisely, an extended area of about 4.5 km in length, located westwards, presents gradual retreat (up to 1 m/year) and net shoreline movement about up to 17 m. In that area, a higher erosion rate of -6.5 m/year is obtained. On the other hand, the most important accretion hotspot is located at the eastern beach, in proximity to the inlets of Keramoti lagoon. There accretion rates reach on average 2.0 m/year and sand accumulation up to 6.9 m.

Table 25. Table with the main statistical parameters for the Gulf of Keramoti.

	SCE	NSM	WLR
Average	11.1	-7.0	-0.8
Min value	2.0	-34.4	-6.5
Max value	34.4	6.9	2.0

Over the latest 5-year period, around 0.054 km² of coastal zone has changed, around 90% of the total land has retreated (-0.049 km²) while only 10% has accumulated (0.005 km²). Significant land loss is observed to the western coast of the Gulf (around -0.023 km²). On the other hand, the area with the higher sand accumulation is located eastwards (around 0.004 km²) (Table 26).

Table 26. Table with the erosion and accretion areas in the Gulf of Keramoti site.

	Area in km²
Net Area Movement	0.054
Erosion	-0.049
Accretion	0.005
Average	-0.005
Max accretion	0.004
Max erosion	-0.043

The sediment transport in this area is primarily affected by the river discharge and the SPM fluxes of Nestos River and secondly by the wave longshore sediment transport. In Keramoti Gulf the sediment transport is westward, with mean value of 150 m³/year and maximum value approximately 264 m³ during 2018-2019. The most energetic years were 2018-2019 and 2016-2017, resulting in the higher shoreline movement. The incident wave energy on the coast for these years was estimated at 51.6 J m⁻¹s⁻¹ and 41.1 J m⁻¹s⁻¹, respectively. On the contrary, low incident wave energy of the order of 5.7 J m⁻¹s⁻¹ was assessed to affect the coastline in 2017-2018, resulting in negligible shoreline movement (0.5 m/year) (Table 27).

Table 27. Table of erosion and Ray Wave model results for the Keramoti gulf study area

Period	Erosion /Accretion (m/yr)	Annual incident wave energy ($\text{J m}^{-1}\text{s}^{-1}$)	Annual Theoretical Sediment Longshore flux (m^3/yr)	Wave Induced Longshore Current (m/s)
2020-2019	-3.2	31.2	-159.9	-0.04
2019-2018	-5.8	51.6	-264.1	-0.05
2018-2017	+0.5	5.7	-34.36	-0.017
2017-2016	+6.8	41.1	-211.2	-0.02
2016-2015	-5.4	11.6	-61.32	-0.005

Focusing on the areas of economic interest:

- a) Erosion dominates the total coastline for the period 2015-2020. The shoreline retreats gradually and extended land is lost at the western part (shoreline retreat up to 15 m in 5 years).

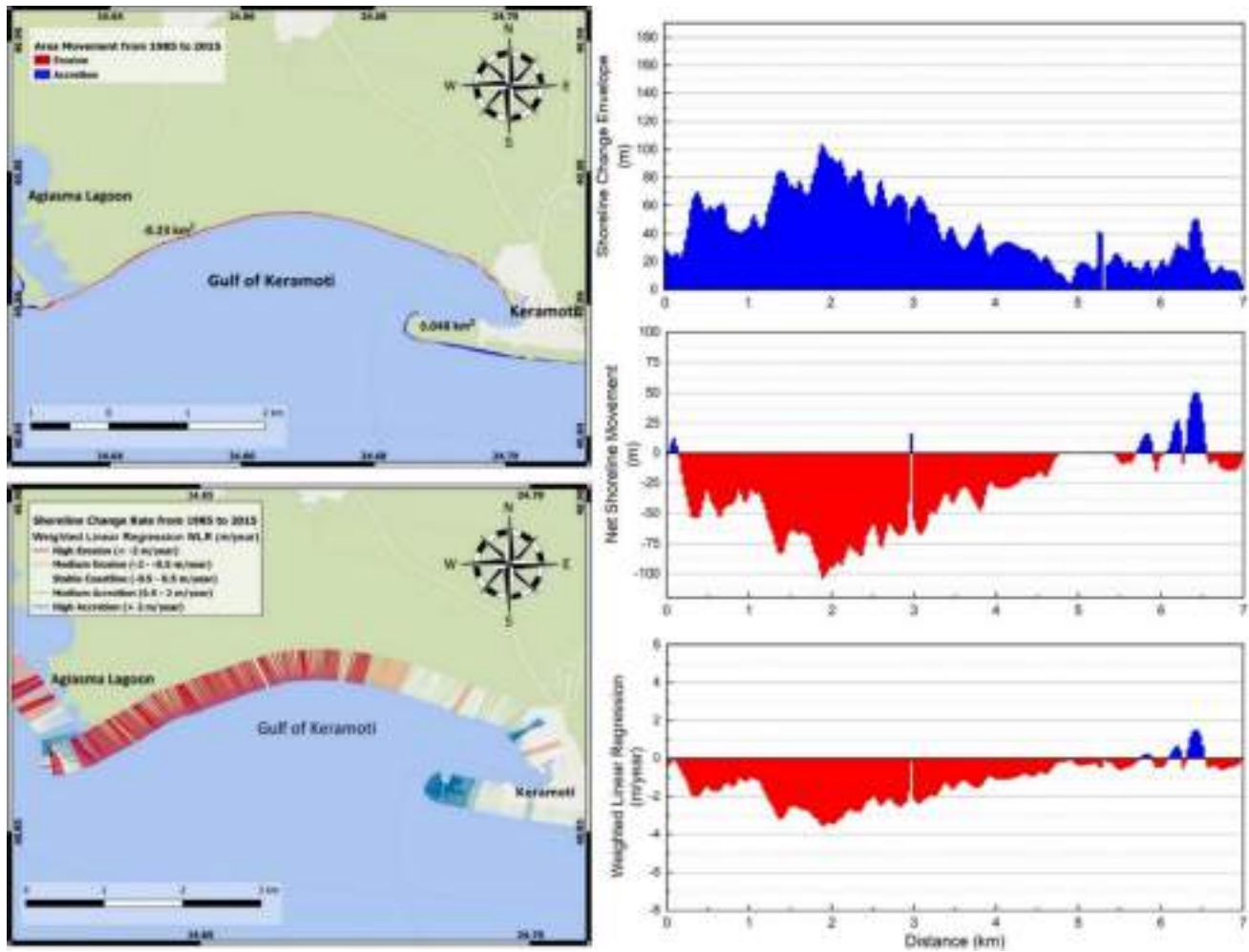


Figure 22. Shoreline evolution from 1985 to 2015. Left panels: a) Map of coastal areal change, and b) Map of the estimated annual shoreline change (WLR). Right panels: The estimated statistical parameters (SCE, NSM, and WLR) per transect along the coastline of Keramoti Gulf.

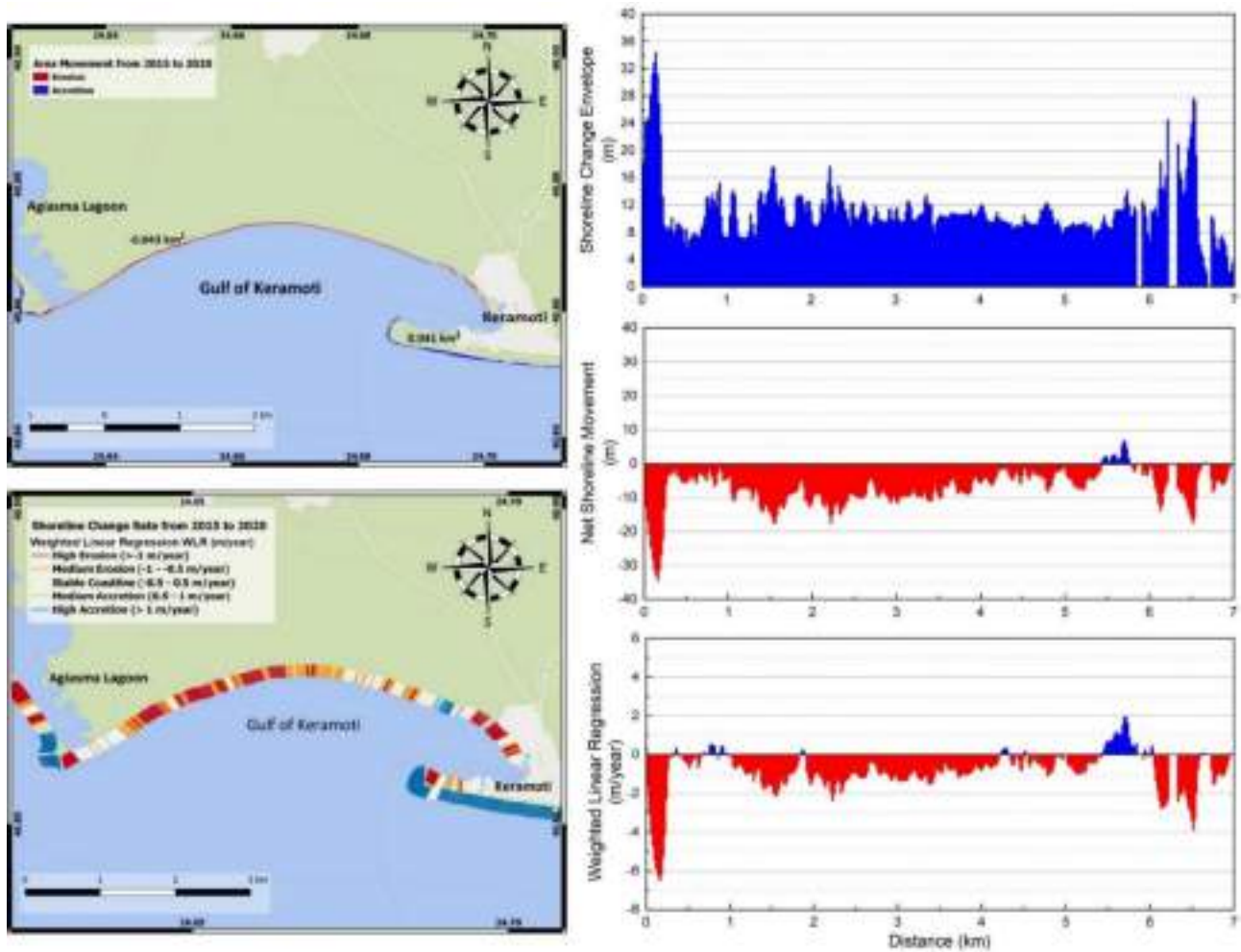


Figure 23. Shoreline evolution from 2015 to 2020. Left panels: a) Map of coastal areal change, and b) Map of the estimated annual shoreline change (WLR). Right panels: The estimated statistical parameters (SCE, NSM, and WLR) per transect along the coastline of Keramoti Gulf.

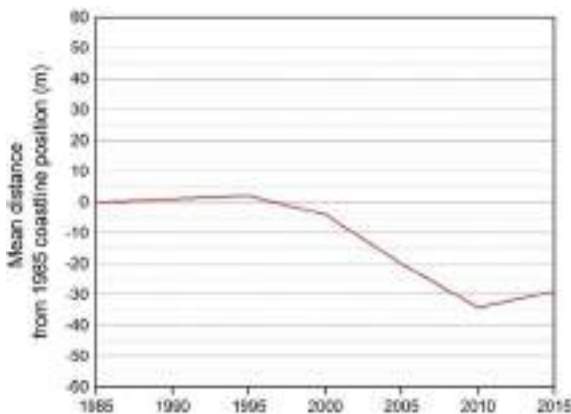
Western Nestos River Delta coastline

The coastal area covering the western coast of Nestos River delta is the third sub-area of interest for this report. It has total length of around 9 km and E-W orientation. It is a long sandy beach having a drainage canal at its center and Nestos River mouth to its east. The Nestos River discharge varies seasonally, and especially after the two dam's construction, the river discharge and the sediment transport are significantly diminished. Changes in the shoreline position have been observed throughout the years. The area is characterized by four hotspots of major land change (two areas of erosion and two of accretion). A chronic gradual change is recorded at these four hotspots from 1985 to 2020. More precisely:

1985-2015

303 transects are used to analyze the statistical parameters along this coast. Figure 24 shows the average shoreline change from 1985 to 2015 with 5-year time increment. From 1985 to 1995, the average shoreline position appears in balance, showing some indication of limited accretion (approximately 0.2 ± 0.3 m/year). Over the next fifteen years (1995 to 2010), the shoreline retreats significantly up to -3.2 ± 0.3 m/year. In the last period (2010-2015), the coastline presents signs of slight accretion, since the mean accretion rate reaches 1.0 ± 0.3 m/year (Table 28). Overall, major shoreline retreat is recorded through this period of the order of -32 m. Two erosion hotspots were identified, located at the central-west and the eastern part. The two areas exhibiting increased accretion rates are located at the western and the central-eastern parts of the study site.

Table 28. Table depicting the mean shoreline change rates per study period.



Class/time frame	No of Transects	Mean (m/year)	Std. Error
2010-2015	303	1.0	0.3
2005-2010	303	-2.8	0.3
2000-2005	303	-3.2	0.3
1995-2000	303	-1.2	0.3
1985-1995	303	0.2	0.3

Figure 24. Temporal variability of the average shoreline position over the period 1985-2015.

Four main hotspots of erosion and accretion along this coastal zone are observed. The average shoreline change (SCE) is around 92 m, the average NSM around -29 m and the average erosion rate around -1.3 m/year (Table 29). More precisely, the higher erosion rates are observed at the shoreline to the eastern end of the area (-7.2 m/year). This dynamic area is the western coast of Nestos River delta, influenced mostly by the limited Nestos River water and SPM fluxes. Seasonal variation in the shoreline position has been found in the area. In this 30-year record, shoreline retreat of up to 241 m was reported. Also, an extended area (about 4 km) covering the zone from Keramoti beach to the main drainage canal presents gradual retreat (up to 5 m/year) and net shoreline movement of up to 150 m. On the other hand, the sandy beach to the west end of the study site (so-called “Ammoglossa”) exhibits significant accretion with rate up to 2.2 m/year and up to 75 m sand accumulation. The second area with considerable sediment accumulation is located to the central-eastern part of the study site. The accretion rate in the area is around 3.7 m/year and the sediment accumulate extending the beach by up to 40 m (Figure 26).

Table 29. Table with the main statistical parameters at the western coast of Nestos River delta.

	SCE	NSM	WLR
Average	91.9	-28.9	-1.3
Min value	21.5	-193.2	-7.2
Max value	241.3	79.8	3.5

Overall, an area of 0.668 km² from the coastal zone has changed throughout these 5-year period. 88% of the total land has been retreated (-0.586 km²) while only 12% has been accumulated (0.082 km²). Significant land loss is observed at the central-western part of the coast in this study site (approximately -0.29 km²), and at the coastline is near the western beach of Nestos delta (around -0.29 km²). On the contrary, the area with the higher sediment accumulation is located at the western end of the study site (approximately 0.048 km²), and the accretion area is located to the central-east of the study site (around -0.014 km²) (Table 30).

Table 30. Table presenting the erosion and accretion zones at the Western part of the Nestos River delta.

	Area in km ²
Net Area Movement	0.668
Erosion	-0.586
Accretion	0.082
Average	-0.036
Max accretion	0.049
Max erosion	0.291

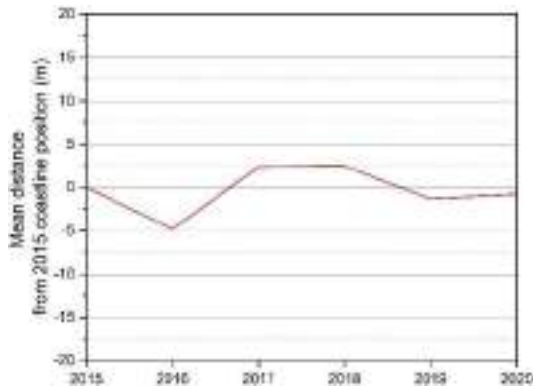
Focusing in areas of economic interest we may summarize that:

- a) The Ammoglossa beach is located to the western end of the shoreline. It is the most accreted beach of the area, with mean shoreline movement of about 60 m and average accretion rates of 1.7 m/year.
- b) Keramoti beach is located to the east of Ammoglossa beach. The western coast is a sandy beach where intense shoreline change take place through these years (SCE: 40-60 m). The average net shoreline movement referring to the period 1985-2015 is about 18 m and the average accretion rate is about 0.30 m/year.
- c) At the eastern part of Keramoti beach, and especially from the Keramoti Military Summer Camp until the drainage canal, high erosion rates are reported ranging from -0.40 up to – 5 m/year. Overall, the shoreline retreats up to -150 m.

2015-2020

The shoreline change statistic parameters are estimated by 445, vertical to the coastline, transects. Figure 25 shows the annual average shoreline change of the total coastal zone from 2015 to 2020. In the first year (2015 to 2016), the average shoreline position retreats around -4.8 m. The following year (2016 to 2017), sediment accumulated to the study area (average NSM 7.2 m). Then, in the period 2017-2018, a minor change is observed, and the coastline is balanced. In 2019 the shoreline retreated again (3.8 m/year), and in 2020 the shoreline balanced again. Theoretically, the total area could be characterized as balanced with minor changes in the average shoreline position. This area consists of four hotspots, and the sediment is transferred from the eroded regions to the regions with accretion. These hotspots are located in the same areas reported in the analysis of 1985-2015.

Table 31. Table of the mean shoreline change rate in periods.



Class/time frame	No of Transects	Mean (m/year)	Std. Error
2019-2020	445	0.6	0.71
2018-2019	445	-3.8	0.56
2017-2018	445	0.1	0.52
2016-2017	445	7.2	0.54
2015-2016	445	-4.8	0.57

Figure 25. Temporal variability of the average shoreline position over the period 2015-2020.

Four main hotspots of erosion and accretion along the coastal zone are observed. The average shoreline change (SCE) is around 28.2 m, with an average NSM around -29 m and an average erosion rate around -2.0 m/year (Table 32). More precisely, the higher erosion rates are observed in the shoreline on the east end (-13.0 m/year). In this 5-years record, shoreline retreat up to 60 m was reported. In addition, an extended area (about 3 km) covering the central-west region of the study site presents gradual retreat (up to 5 m/year) and net shoreline movement up to 30 m. On the other hand, the sandy beach on the west end of the study site presents a significant accretion rate of up to 6 m/year and up to 42 m sediment accumulation. The second area with considerable sediment accumulation is located in the central-east of the study site with an accretion rate of around 4 m/years and sediment accumulation up to 40 m. The length of that area is estimated at about 2.5 km.

Table 32. Table with the main statistical parameters for the West Nestos river estuaries.

	SCE	NSM	WLR
Average	28.2	-0.7	0.2
Min value	9.1	-59.9	-13.0
Max value	62.4	43.4	9.1

Approximately 0.054 km² of the coastal zone has changed through this period. 53% of the total land has been retreated (-0.049 km²) and 47% has been accumulated (0.005 km²), thus the area is balanced in terms of sediment budget. Significant land loss is observed at the central-western coast of the study site (around -0.29 km²) and at the coastline near the western Nestos River mouth (approximately -0.29 km²). On the other hand, the area with the higher sediment accumulation lies to the western end of the study site (about 0.048 km²), while another accretion zone is located at the central-eastern part of the study site (around -0.014 km²) (Table 33).

Table 33. Table showing the erosion/accretion zones at the Western Coast of Nestos River delta.

	Area in km ²
Net Area Movement	0.054
Erosion	-0.049
Accretion	0.005
Average	-0.005
Max accretion	0.004
Max erosion	-0.043

The sediment influx is directly linked to the Nestos River discharge and the SPM transport from the river mouth. At the western Nestos River delta, sediment moves from east to west, transporting on average 795 m³/year, peaking at 904 m³/year in 2018-2019. The most energetic periods were 2018-2019 (incident wave energy equal to 181.23 J m⁻¹s⁻¹), leading to significant shoreline retreat (about -3.8 m/year). The sedimentation in that area is strongly affected by the river sediment transport, and the ray wave model can only explain the longshore sediment transport (from east to west) and redistribution.

Table 34. Erosion rates and Ray-Wave model results for the West Coastline of Nestos River delta.

Period	Erosion (m/yr)	Annual incident wave energy (J m ⁻¹ s ⁻¹)	Annual Theoretical Sediment Longshore flux (m ³ /yr)	Wave Induced Longshore Current (m/s)
2020-2019	0.6	153.82	758.56	0.395
2019-2018	-3.8	181.23	903.99	0.388
2018-2017	0.1	158.51	785.24	0.329
2017-2016	7.2	150.02	747.79	0.348
2016-2015	-4.8	158.48	782.09	0.347

Focusing on the areas of economic interest:

- a) The Ammoglossa beach continues the accretion trend observed from the 1985-2015 analysis. This period, the shoreline movement ranges from 10-20 m and the average accretion rate is about 2 m/year.

- b) Keramoti beach is located to the east of Ammoglossa beach. The west coast is a sandy beach with intense shoreline changes through the years (SCE: 10-40 m). The average net shoreline movement (referring to the period 2015-2020) is about 20 m, with average accretion rate of about 4 m/year.
- c) To the eastern part of Keramoti beach, and especially from the Keramoti Military Summer Camp until the drainage canal high erosion rates are reported ranging from -0.40 up to - 5 m/year. The shoreline retreats by up to -30 m.

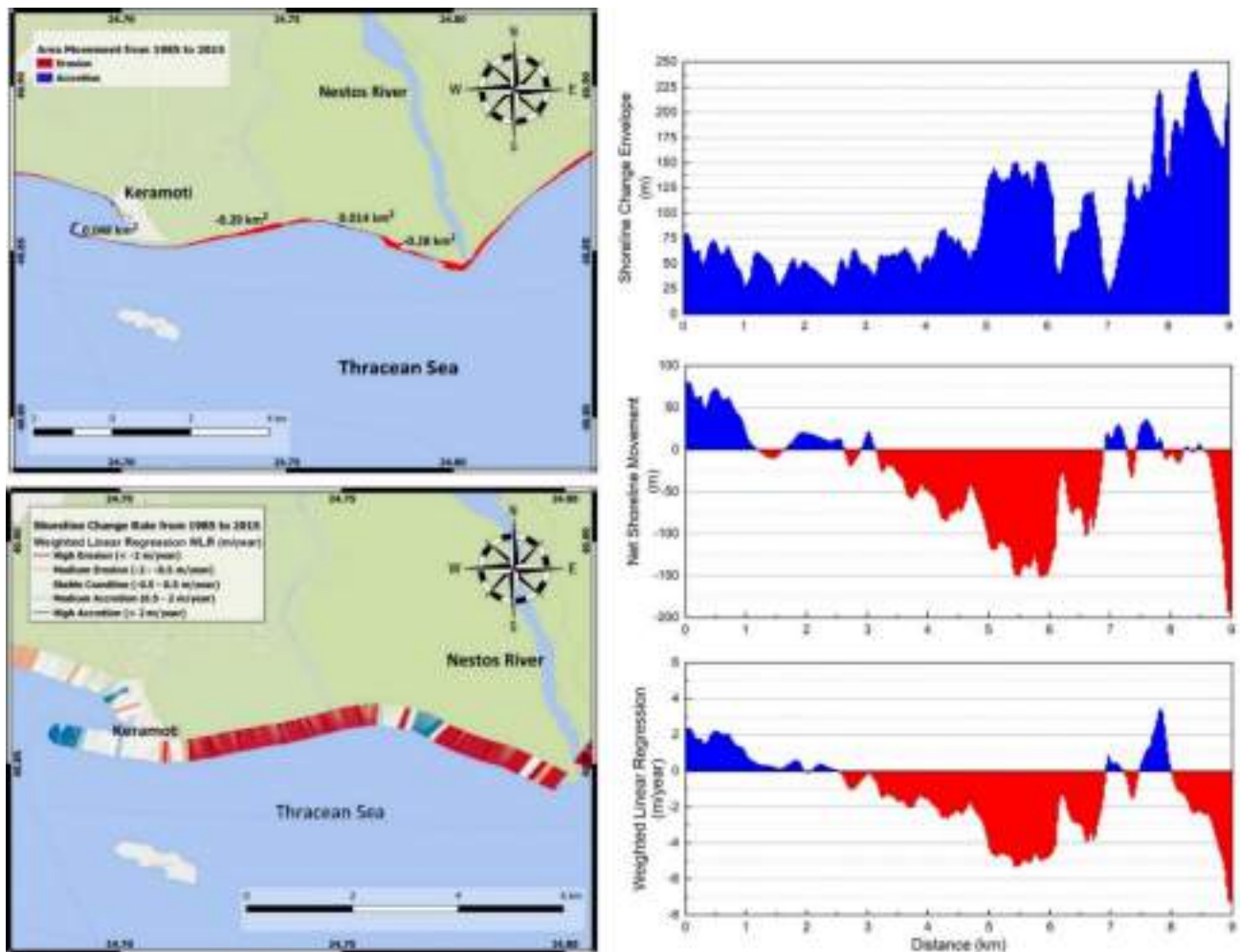


Figure 26. Shoreline evolution from 1985 to 2015. Left panel: a) Map of coastal areal change, and b) Map of the estimated annual shoreline change (WLR). Right panels: The estimated statistical parameters (SCE, NSM, and WLR) per transect along the Western Coast of Nestos River delta.

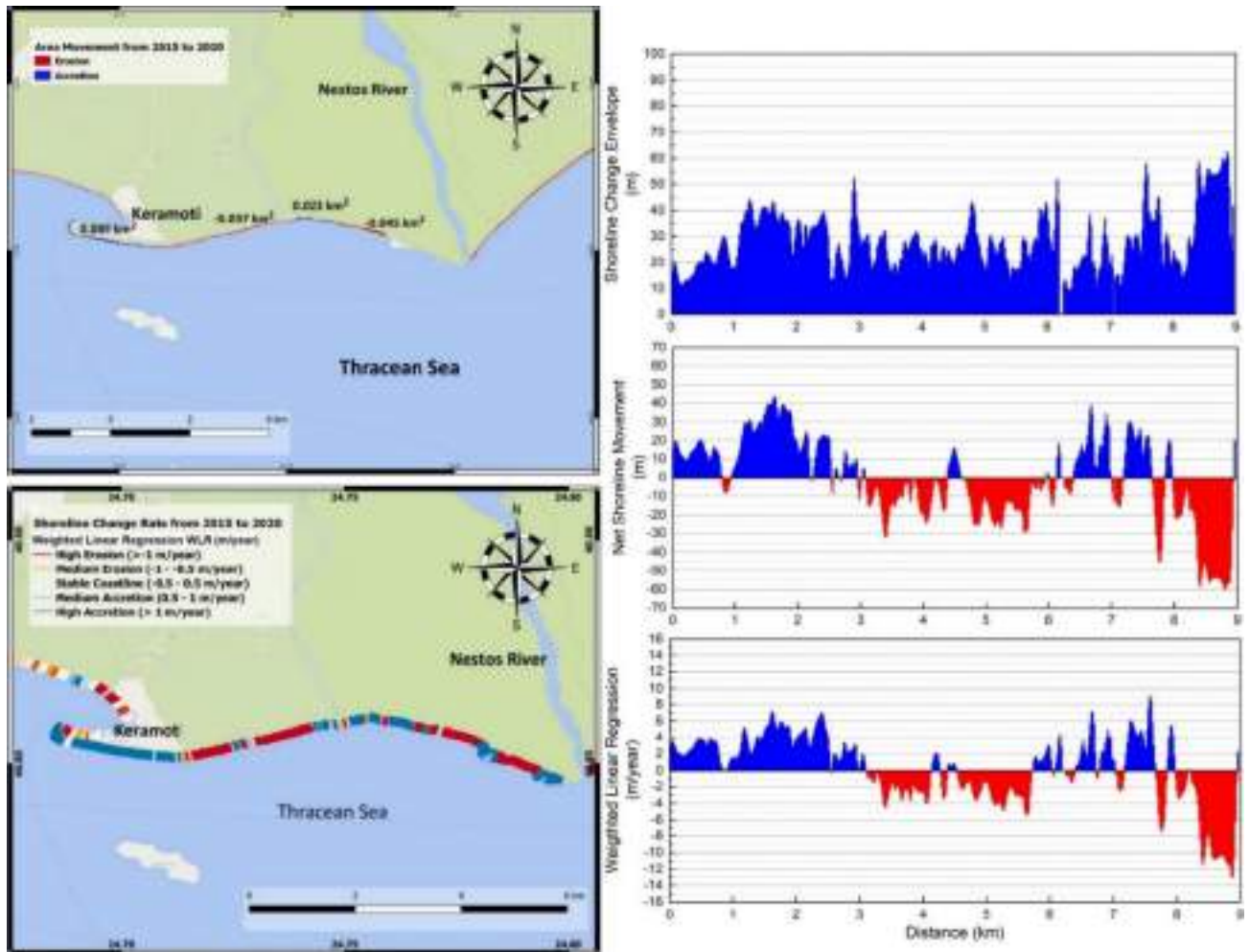


Figure 27. Shoreline evolution from 2015 to 2020. Left panels: a) Map of coastal area change, and b) Map of the estimated annual shoreline change (WLR). Right panels: The estimated statistical parameters (SCE, NSM, and WLR) per transect along the Western Coast of Nestos River delta.

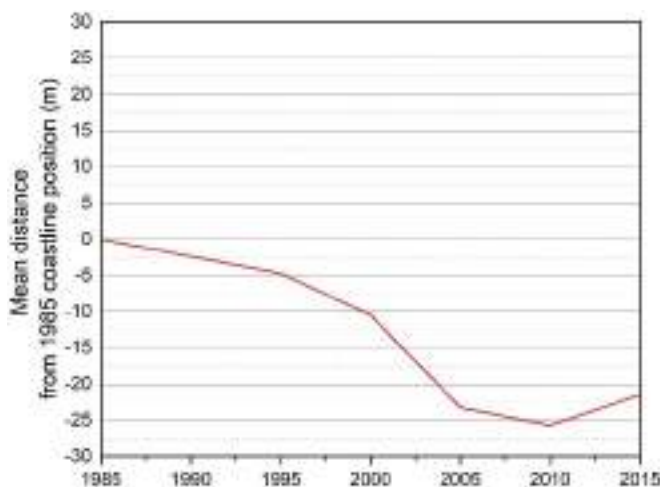
East Coast of Nestos River delta

The coastal area to the east of Nestos River delta is the longest sub-area of all other study sites. It has total length of around 17 km and SW-NE orientation. As mentioned above, the Nestos river discharge varies seasonally, and especially after the construction of the two hydropower dams, the river discharge and the sediment transport have been significantly diminished. The sediment transport reduction results in significant changes in the shoreline position, especially at the regions close to the Nestos River mouth. At the eastern Nestos River delta sub-area, there are four highly-touristic beaches (Erasmio, Maggana, Myrodato, Skala Avdiron). Their protection from erosion events is crucial for the local economy. A gradual shoreline retreat characterizes the southwest part of the study site over the study years, but accretion dominates the northeast part. More precisely:

1985-2015

The shoreline change statistic parameters are estimated by 572, vertical to the coastline, transects. Figure 28 shows the average shoreline change of the total coastal zone from 1985 to 2015 in five years period. More precisely, from 1985 to 2010, the average shoreline position retreats by up to 26 m, with shoreline erosion rate up to -2.6 m/year. In the next five-year period (2010 – 2015), slight accretion (around 0.8 ± 0.1 m/year) is observed. Overall, the Eastern Coast of Nestos delta suffers from chronic erosion, due to the high and continuous shoreline retreat in the area.

Table 35. Table of the mean shoreline change rate in periods.



Class/time frame	No of Transects	Mean (m/year)	Std. Error
2010-2015	572	0.8	0.1
2005-2010	572	-0.5	0.1
2000-2005	572	-2.6	0.1
1995-2000	572	-1.1	0.1
1985-1995	572	-0.5	0.1

Figure 28. Temporal variability of the average shoreline position over the period 1985-2015.

The average shoreline change (SCE) in this sub-area is approximately 40.2 m, the average NSM reaches -21.5 m and the average erosion rate almost -0.9 m/year (Table

36). More precisely, the higher erosion rates are observed at the coastal area eastwards of Nestos River mouth (~ -3.4 m/year). Over this 30-year record, shoreline retreat up to -106 m was reported. To the north-east part of the coast, the coastline seems balanced with low accretion and erosion rates (up to ± 1 m/y). The beaches exhibiting the higher sediment accumulation are located at the eastern and western sides of the Erasmio lagoon inlet. At this zone, the accretion rates is as high as $+0.6$ m/year and the mean NSM about 30 m (Figure 30).

Table 36. Main statistical parameters for the coastline to the East of Nestos River mouth.

	SCE	NSM	WLR
Average	40.2	-21.5	-0.9
Min value	1.1	-106.1	-3.4
Max value	106.1	44.3	1.2

Throughout these 30 years, around 0.532 km² of coastal zone has been altered due to coastal process prevailing in the area. 84% of this area has been retreated (-0.449 km²) and 16% has been accumulated (0.083 km²). Significant land loss is observed to the central-western coast of the study site (around -0.29 km²), and at the coastline near the eastern Nestos deltaic coast (approximately -0.449 km²). On the other hand, the area with the higher sediment accumulation is located about 2 km westwards, at the Myrtofyto beach (about 0.036 km²) (Table 37).

Table 37. Erosion and accretion areas along the Eastern Coast of Nestos River delta.

	Area in km ²
Net Area Movement	0.532
Erosion	-0.449
Accretion	0.083
Average	-0.008
Max accretion	0.036
Max erosion	-0.283

Focusing on the touristic hotspots we may summarize the following:

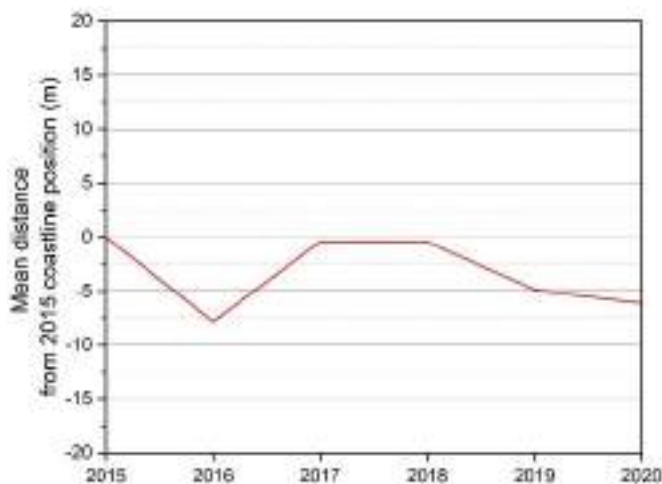
- a) The Erasmio beach exhibits high erosion rates (up to -2.2 m/year), thus the shoreline retreated by around 60 m.
- c) The Maggana beach illustrates mean erosion rate ~ 0.2 m/year, and the shoreline retreated by up to 35 m.

- d) At Myrtofyto beach, the central part of the beach presents up to 20 m erosion, with an average rate of -0.5 m/year. Slight accretion is observed at the eastern part of the beach, with an average accretion rate of about 0.15 m/year.
- e) The beach at Skala Avdiron seems stabilized with low accretion or erosion rates and negligible net shoreline movement.

2015-2020

The statistical parameters describing shoreline change in this sub-area are based on the movement of coast along 852 transects perpendicular to the coast. Figure 29 demonstrates the temporal variability in mean annual shoreline change during the 2015-2020 period. In the first year (2015 to 2016), the mean shoreline position retreats by around -7.8 m. In the period 2016 - 2017, significant sediment accretion is observed (mean shoreline movement of 7.5 m), while in 2017-2018 the coastline appears balanced. In 2019 the shoreline retreated again by 4.4 m/year and in 2020 slight erosion (-1.3 m) prevailed (Table 36). Theoretically, the total area could be characterized as balanced with minor changes in the average shoreline position. This area consists of two hotspots, and the sediment is transferred from the eroded regions to the regions with accretion. These hotspots are located at the same areas reported in the analysis of 1985-2015.

Table 38. Temporal variability in the mean shoreline change rates per year.



Class/time frame	No of Transects	Mean (m/year)	Std. Error
2019-2020	852	-1.3	0.22
2018-2019	852	-4.4	0.21
2017-2018	852	0.0	0.23
2016-2017	852	7.5	0.25
2015-2016	852	-7.8	0.29

Figure 29. Temporal variability of the average shoreline position over the period 2015-2020.

The average shoreline change (SCE) is around 19 m, the mean NSM is approximately 6.1 m and the average accretion rate reached 0.6 m/year. High erosion is observed in an extended area of about 7 km in length, extending from Nestos River mouth to Erasmio beach. At this area, high erosion rates (up to -18.8 m/year) are observed, and the shoreline retreated by up to -113.5 m. On the other hand, the central-east shoreline (around 9 km) shows significant sediment accumulation, with accretion rates of up to 6.2 m/year and maximum net shoreline movement of up to 31.5 m. The areas with the higher accretion rate are located at the eastern end of Eratino beach (WLR: 1-2.6 m/year), at Maggana Beach (WLR: 1.5-6.2 m/year), and at the western part of Myrtofyto beach (WLR: 1-5.0 m/year).

Table 39. Main statistical parameters for the Eastern Coast of Nestos River delta.

	SCE	NSM	WLR
Average	-19.0	6.1	0.6
Min value	2.7	-113.5	-18.8
Max value	113.5	31.5	6.2

Over this 5-year period, approximately 0.159 km² of the coastal zone have been altered. Of this area, about 53% has been retreated, representing -0.085 km² while 47% has been accumulated (or 0.074 km²). Significant land loss is observed at the coastline between Nestos river mouth and Erasmio beach (around -0.12 km²). On the other hand, the area with the higher sediment accumulation is the Maggana beach (about 0.048 km²) and the western part of Myrtofyto beach (around 0.022 km²) (Table 40).

Table 40. Erosion and accretion areas along the Eastern Coast of Nestos River delta.

	Area in km ²
Net Area Movement	0.159
Erosion	-0.085
Accretion	0.074
Average	0.000
Max accretion	0.033
Max erosion	-0.038

The sediment transport in this area appears strongly linked to the Nestos River discharge and SPM fluxes, as well as to the wave-induced longshore sediment transport. To the east of Nestos River delta, sediment moves eastwards with mean sediment transport of approximately 240 m³/year. The maximum sediment transport has been estimated in the 2018-2019 period of about 383 m³/year. The most energetic periods are 2018-2019 (74.88 J m⁻¹s⁻¹) and 2016-2017 (65.24 J m⁻¹s⁻¹), resulting in high shoreline movement. On the other hand, the low incident wave energy (3.8 J m⁻¹s⁻¹) in 2017-2018 results in negligible shoreline movement (almost zero erosion rate).

Table 41. Erosion rates and Ray-Wave model results for the Eastern Coast of Nestos River delta.

Period	Erosion Rate (m/yr)	Annual Longshore Wave Power ($\text{J m}^{-1}\text{s}^{-1}$)	Annual Theoretical Sediment Longshore flux (m^3/yr)	Wave Induced Longshore Current (m/s)
2020-2019	-1.3	59.78	301.33	0.241
2019-2018	-4.4	74.88	382.75	0.228
2018-2017	0.0	3.08	18.77	0.166
2017-2016	7.5	65.24	332.56	0.205
2016-2015	-7.8	31.33	159.8	0.172

Focusing on the touristic hotspots:

- a) The Erasmio beach is divided into four sections according to its erosion activity. The higher shoreline retreat (up to -18 m) is presented at the central western part of the beach, showing rate up to -2.6 m/year.
- b) The Maggana beach illustrates shoreline accretion of up to 20 m in 2015-2020.
- c) The Myrtofyto beach, exhibits shoreline accretion ranging between 5 and 10 m in the period 2015-2020.
- d) At the central part of the Skala Avdiron beach, shoreline retreat of up to 20 m is observed. On the other hand, at the western and eastern parts of the Skala Avdiron beach, accretion (average accretion about 5 m) is reported.

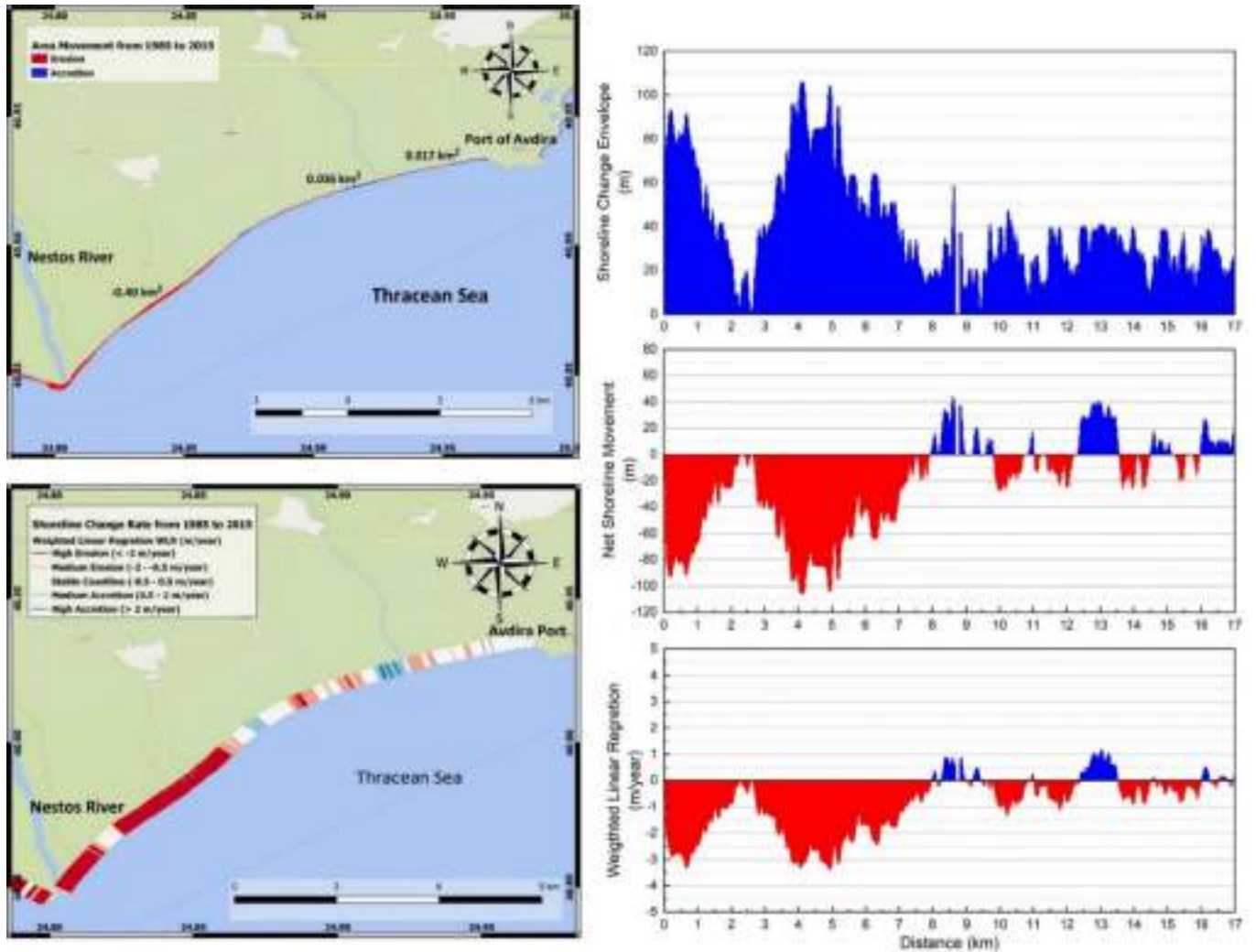


Figure 30. Shoreline evolution from 1985 to 2015. Left panels: a) Map of coastal areal change, and b) Map of the estimated annual shoreline change (WLR). Right panels: The estimated statistical parameters (SCE, NSM, and WLR) per transect along the Eastern Coast of Nestos River delta.

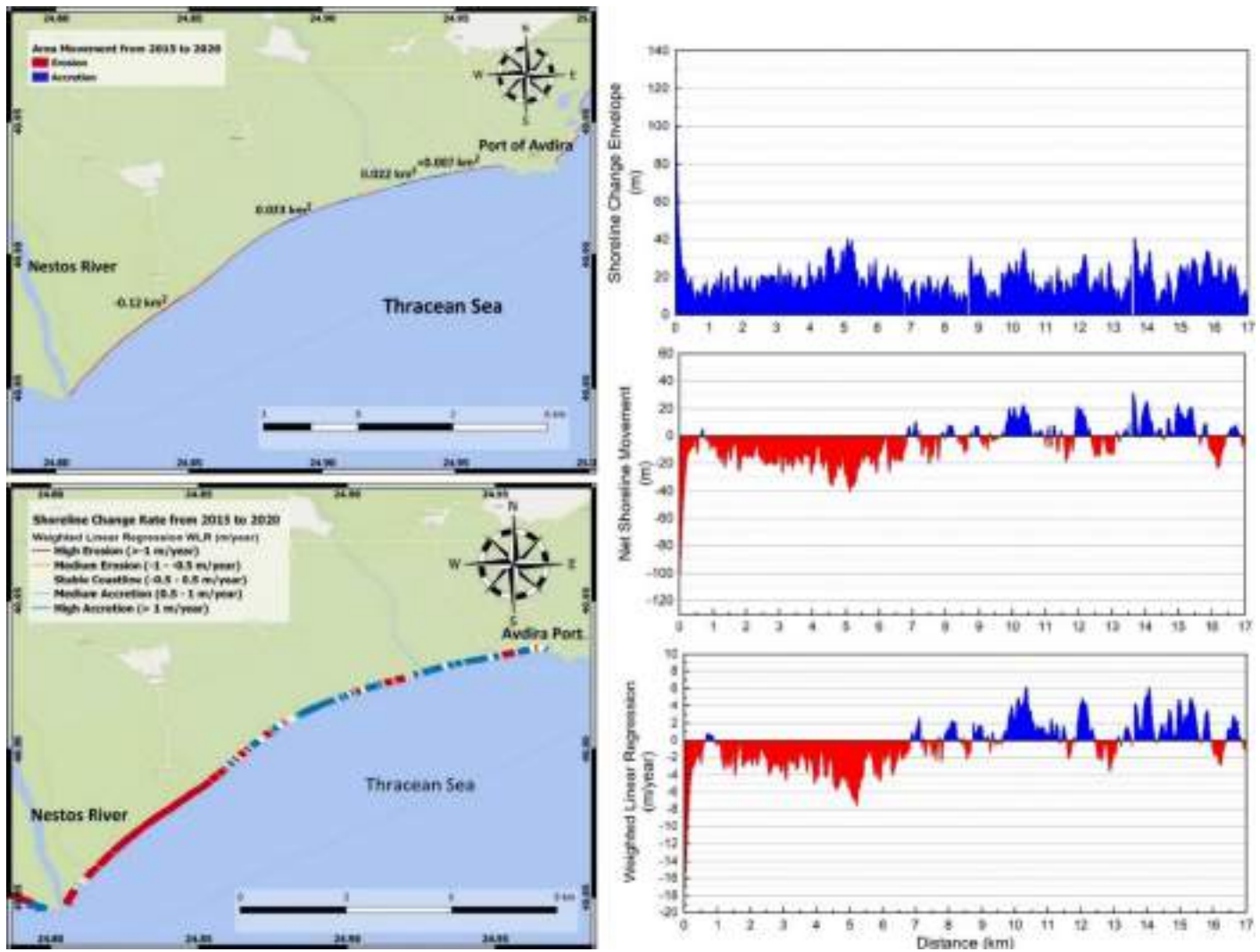


Figure 31. Shoreline evolution from 2015 to 2020. Left panels: a) Map of coastal areal change, and b) Map of the estimated annual shoreline change (WLR). Right panels: The estimated statistical parameters (SCE, NSM, and WLR) per transect along the Eastern Coast of Nestos River delta.

The effect of Nestos River damming on the Nestos deltaic coastal zone

In conclusion, the higher shoreline retreat in the entire study site is evident from 2015 and onwards. Nestos River dams were constructed in 1996 and started operating in 1998. After their construction, river flow to the coastal zone has been stabilized, ranging from 20-30 m³/s, while the SPM flux has been diminished. Figure 11 shows a clear downward trend in the plume area (around 80%) since the dams' construction upstream of the river. The plume area is directly linked to the river discharge. The constant low discharge rates in the Nestos river influence the sediment transport in the river estuaries, leading to coastal erosion events.

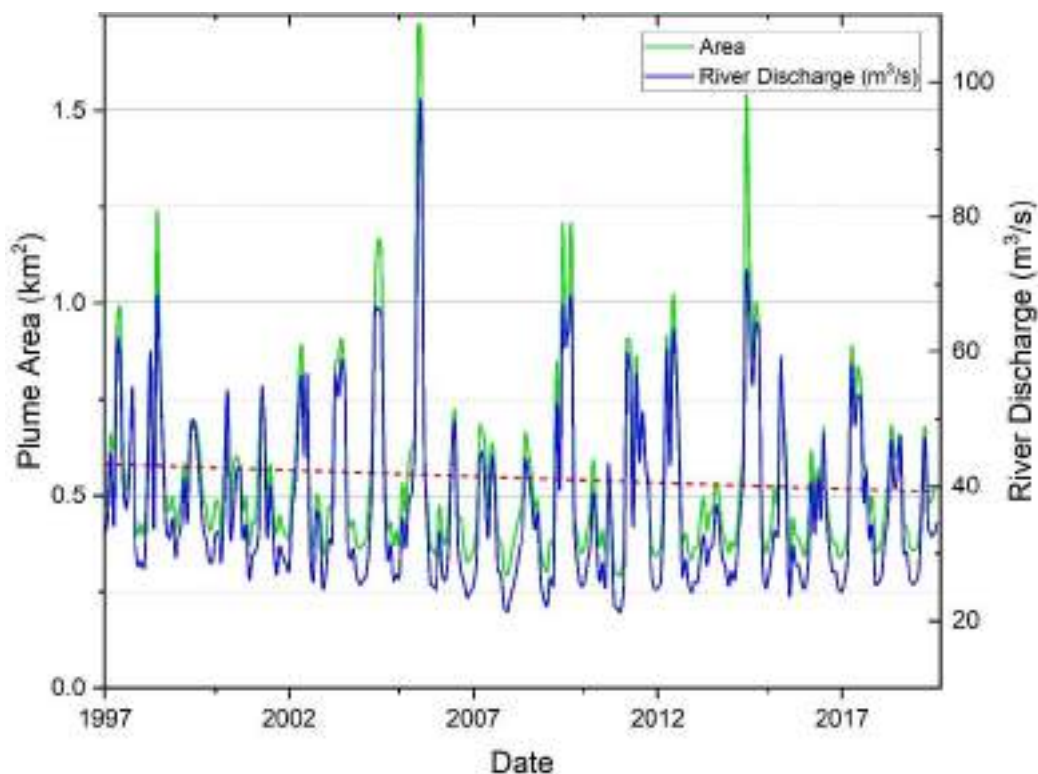


Figure 32. Plume area and river discharge of Nestos river

Figure 33 presents the erosion and accretion areas of the entire study site, from 1995 to 2020. About 0.85 km² of sandy beaches in this zone has been eroded over this 25-year period. Approximately 0.15 km² have been lost at the Keramoti Gulf, nearly 0.23 km² at the western coast of Nestos River delta, and more than 0.35 km² at the eastern coast of Nestos River delta (Figure 33).

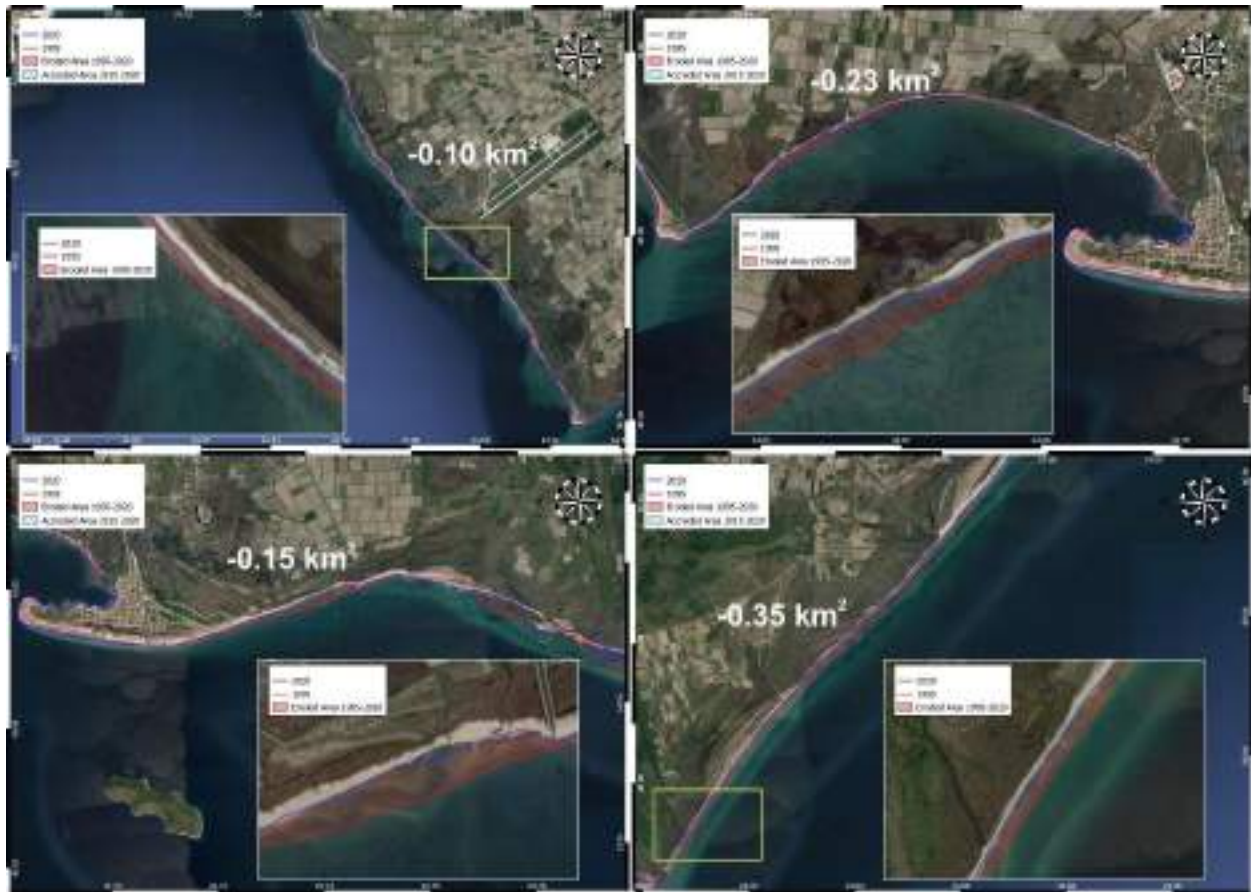


Figure 33. Estimated Eroded Area along the Nestos River deltaic zone from 1995 to 2020.

References

- Alexander, P. S., & Holman, R. A. (2004). Quantification of nearshore morphology based on video imaging. *Marine geology*, 208(1), 101-111.
- Anderson, K., & Gaston, K. J. (2013). Lightweight unmanned aerial vehicles will revolutionize spatial ecology. *Frontiers in Ecology and the Environment*, 11(3), 138-146.
- Andreadaki, M., Hrisanthou, V., & Kotsovinos, N. (2008, October). Calculation of sediment reduction at the outlet of Nestos river basin due to the dams. In IV International Symposium on Transboundary Waters Management, Thessaloniki, Greece (pp. 15-18).
- Anfuso, G., Pranzini, E., & Vitale, G. (2011). An integrated approach to coastal erosion problems in northern Tuscany (Italy): Littoral morphological evolution and cell distribution. *Geomorphology*, 129(3-4), 204-214.
- Arheimer, B., Lindström, G., & Olsson, J. (2011). A systematic review of sensitivities in the Swedish flood-forecasting system. *Atmospheric Research*, 100(2-3), 275-284.
- Boskidis, I., Gikas, G. D., Sylaios, G., & Tsihrintzis, V. A. (2011). Water quantity and quality assessment of lower Nestos river, Greece. *Journal of Environmental Science and Health, Part A*, 46(10), 1050-1067.
- Bouchahma, M., & Yan, W. (2012). Automatic measurement of shoreline change on Djerba Island of Tunisia. *Computer and Information Science*, 5(5), 17.
- Braud, D. H., & Feng, W. (1998). Semi-automated construction of the Louisiana coastline digital land/water boundary using Landsat Thematic Mapper satellite imagery. Louisiana Applied Oil Spill Research and Development Program, OS2 RAPD Technical Report Series, 97(002).
- Colomina, I., & Molina, P. (2014). Unmanned aerial systems for photogrammetry and remote sensing: A review. *ISPRS Journal of photogrammetry and remote sensing*, 92, 79-97.
- Congedo, L. (2016). Semi-automatic classification plugin documentation. Release, 4(0.1), 29.
- Conispoliatis, N., & Lykousis, V. (1986). Mineralogy of the surficial sediments of Kavala Bay, northern Aegean Sea. *Estuarine Coastal and Shelf Science*, 23(5), 739-749.
- Dolan, R. J., & Jeuland, A. P. (1981). Experience curves and dynamic demand models: Implications for optimal pricing strategies. *Journal of Marketing*, 45(1), 52-62.
- Everaerts, J. (2008). The use of unmanned aerial vehicles (UAVs) for remote sensing and mapping. *The International Archives of the Photogrammetry, Remote Sensing and Spatial Information Sciences*, 37(2008), 1187-1192.

- Floreano, D., & Wood, R. J. (2015). Science, technology and the future of small autonomous drones. *Nature*, 521(7553), 460-466.
- Frazier, P. S., & Page, K. J. (2000). Water body detection and delineation with Landsat TM data. *Photogrammetric engineering and remote sensing*, 66(12), 1461-1468.
- Genz, A. S., Fletcher, C. H., Dunn, R. A., Frazer, L. N., & Rooney, J. J. (2007). The predictive accuracy of shoreline change rate methods and alongshore beach variation on Maui, Hawaii. *Journal of Coastal Research*, 23(1), 87-105.
- Hapke, C., & Richmond, B. (2000). Monitoring beach morphology changes using small-format aerial photography and digital softcopy photogrammetry. *Environmental Geosciences*, 7(1), 32-37.
- Harley, M. D., Turner, I. L., Short, A. D., & Ranasinghe, R. (2011). Assessment and integration of conventional, RTK-GPS and image-derived beach survey methods for daily to decadal coastal monitoring. *Coastal Engineering*, 58(2), 194-205.
- Kamidis, N., Sylaios, G., & Tsihrintzis, V. A. (2011). Modeling the Nestos River plume dynamics using ELCOM. *Desalination and Water Treatment*, 33(1-3), 22-35.
- Kroon, A., Davidson, M.A., Aarninkhof, S.G.J., Archetti, R., Armaroli, C., Gonzalez, M., Medri, S., Osorio, A., Aagaard, T., Holman, R.A., Spanhoff, R. (2007). Application of remote sensing video systems to coastline management problems. *Coastal Engineering*, 54(6-7), 493-505.
- Kuleli, T. (2010). Quantitative analysis of shoreline changes at the Mediterranean Coast in Turkey. *Environmental monitoring and assessment*, 167(1-4), 387-397.
- Kuleli, T., Guneroglu, A., Karsli, F., & Dihkan, M. (2011). Automatic detection of shoreline change on coastal Ramsar wetlands of Turkey. *Ocean Engineering*, 38(10), 1141-1149.
- Lalechos, N., & Savoyat, E. (1977). La sedimentation néogène dans le fosse Nord Egéen. *Proceedings of the VI Colloquium on the Geology of the Aegean Region*. Institute of Geological and Mining Research, 2, 591-603.
- Lee, J. M., Park, J. Y., & Choi, J. Y. (2013). Evaluation of sub-aerial topographic surveying techniques using total station and RTK-GPS for applications in macrotidal sand beach environment. *Journal of Coastal Research*, 65(1), 535-540.
- Lindström, G., Pers, C., Rosberg, J., Strömqvist, J., & Arheimer, B. (2010). Development and testing of the HYPE (Hydrological Predictions for the Environment) water quality model for different spatial scales. *Hydrology research*, 41(3-4), 295-319.
- Louati M., Saïdi H., & Zargouni F. (2015). Shoreline change assessment using remote sensing and GIS techniques: a case study of the Medjerda delta coast Tunisia (2015), 4239-4255

- McFeeters, S. K. (1996). The use of the Normalized Difference Water Index (NDWI) in the delineation of open water features. *International journal of remote sensing*, 17(7), 1425-1432.
- Mills, M. J., Toon, O. B., & Thomas, G. E. (2005). Mesospheric sulfate aerosol layer. *Journal of Geophysical Research: Atmospheres*, 110(D24).
- Morton, R. A., Leach, M. P., Paine, J. G., & Cardoza, M. A. (1993). Monitoring beach changes using GPS surveying techniques. *Journal of Coastal Research*, 702-720.
- Natesan, U., Thulasiraman, N., Deepthi, K., & Kathiravan, K. (2013). Shoreline change analysis of Vedaranyam coast, Tamil Nadu, India. *Environmental Monitoring and Assessment*, 185(6), 5099-5109.
- Proedrou, P. (1979). The evaporites formation in the Nestos-Prinos graben in the Northern Aegean Sea. *Ann. Geol. Pays Helle*, (2), 1013-1020.
- Psilovikos, A., Vavliakis, E., & Langalis, T. (1988). Natural and anthropogenic processes of the recent evolution of Nestos delta. *Bulletin of the Geological Society of Greece*, 20, 313-324.
- Pye, K., & Blott, S. J. (2016). Assessment of beach and dune erosion and accretion using LiDAR: Impact of the stormy 2013–14 winter and longer-term trends on the Sefton Coast, UK. *Geomorphology*, 266, 146-167.
- Rasuly, A., Naghdifar, R., & Rasoli, M. (2010). Monitoring of Caspian Sea coastline changes using object-oriented techniques. *Procedia Environmental Sciences*, 2, 416-426.
- Saye, S. E., Van der Wal, D., Pye, K., & Blott, S. J. (2005). Beach–dune morphological relationships and erosion/accretion: an investigation at five sites in England and Wales using LIDAR data. *Geomorphology*, 72(1-4), 128-155.
- Stockdonf, H. F., Sallenger Jr, A. H., List, J. H., & Holman, R. A. (2002). Estimation of shoreline position and change using airborne topographic lidar data. *Journal of Coastal Research*, 502-513.
- Sylaios, G. K., Anastasiou, S., & Tsihrintzis, V. A. (2012). Restoration of a seashore eroded due to dam operation through beach nourishment. *Ecohydrology & Hydrobiology*, 12(2), 123-135.
- Sylaios, G., Stamatis, N., Kallianiotis, A., & Vidoris, P. (2005). Monitoring water quality and assessment of land-based nutrient loadings and cycling in Kavala Gulf. *Water Resources Management*, 19(6), 713-735.
- Taborda, R., & Silva, A. (2012). COSMOS: A lightweight coastal video monitoring system. *Computers & Geosciences*, 49, 248-255.
- Takaku, J., Tadono, T., & Tsutsui, K. (2014) Generation of high resolution global DSM from ALOS PRISM. *ISPRS Annals of Photogrammetry, Remote Sensing & Spatial Information Sciences*, 2(4).

- Theuerkauf, E. J., & Rodriguez, A. B. (2012). Impacts of transect location and variations in along-beach morphology on measuring volume change. *Journal of Coastal Research*, 28(3), 707-718.
- Thieler, E. R., Himmelstoss, E. A., Zichichi, J. L., & Ergul, A. (2009). The Digital Shoreline Analysis System (DSAS) version 4.0-an ArcGIS extension for calculating shoreline change (No. 2008-1278). US Geological Survey.
- Turki, I., Medina, R., Coco, G., & Gonzalez, M. (2013). An equilibrium model to predict shoreline rotation of pocket beaches. *Marine Geology*, 346, 220-232.
- Van Rijn, L. C., & Kroon, A. (1993). Sediment transport by currents and waves. *Proceedings of the Coastal Engineering Conference*, 3, 2613-2628.
- Young, A. P., & Ashford, S. A. (2006). Application of airborne LIDAR for Seacliff volumetric change and beach-sediment budget contributions. *Journal of Coastal Research*, 307-318.
- Williams, A.T., Rangel-Buitrago, N., Pranzini, E., & Anfuso, G. (2018). The management of coastal erosion. *Ocean & Coastal Management* 156, 4-20, <https://doi.org/10.1016/j.ocecoaman.2017.03.022>.
- Zhang, K., Douglas, B.C., & Leatherman, S.P. (2004). Global warming and coastal erosion. *Climatic Change* 64, 41-58, <https://doi.org/10.1023/B:CLIM.0000024690.32682.48>.
- Salman, A., Lombardo, S., Doody, P., 2004. Living with coastal erosion in Europe: Sediment and Space for Sustainability. EuroSION project, "Coastal erosion – Evaluation of the need for action", DG Environment, European Commission.